Applied Physics A (2026) 132:231
https://doi.org/10.1007/s00339-026-09421-5

Applied Physics A
Materials Science & Processing

Role of La/Ce co-substitution in modulating conductivity and interfacial polarization in hard-soft $CoFe_2O_4/NiFe_2O_4$ spinel ferrite nanocomposites [H/S $CoLa_xCe_xFe_{2-2x}O_4/NiFe_2O_4$ ($x \leq 0.10$) SFNCs]

A. Baykal[1,2] · B. Ünal[3] · M. A. Almessiere[4,5] · A. Demir Korkmaz[6] · Y. Slimani[4]

Received: 20 November 2025 / Accepted: 9 February 2026
© The Author(s) 2026

Abstract

Hard/soft spinel ferrite nanocomposites H/S $CoLa_xCe_xFe_{2-2x}O_4/NiFe_2O_4$ ($x \leq 0.10$) SFNCs were successfully prepared using a sol–gel auto-combustion method to systematically investigate the influence of La/Ce co-substitution, frequency, and temperature on their structural, electrical, and dielectric properties. XRD, SEM, TEM, HR-TEM, and EDX analyses confirmed the formation of the spinel phases and nanocomposite morphology, while revealing a systematic reduction in crystallite size from ~43.44 nm ($x = 0.00$) to ~26.11 nm ($x = 0.10$), attributed to rare-earth-ion-induced grain-boundary pinning. Broadband dielectric spectroscopy, complex impedance (Z*), and electric modulus (M*) analyses reveal strong frequency dispersion and thermally activated behavior governed by hopping conduction, space-charge effects, and defect-assisted relaxation. AC and DC conductivity results identify an optimal substitution range ($x \approx 0.06$–0.08), where thermally assisted charge transport is maximized and activation energy is minimized. In contrast, excessive substitution ($x = 0.10$) introduces structural disorder and insulating grain boundaries, leading to reduced mobility and increased resistivity. Dielectric loss and three-dimensional ε″ analyses demonstrate a clear transition from bulk-dominated dissipation at low substitution levels to relaxation-dominated behavior at $x \geq 0.08$, associated with enhanced Maxwell–Wagner interfacial polarization. Impedance spectroscopy reveals a crossover from grain-controlled to grain-boundary-dominated transport, confirmed by the emergence of multiple semicircular arcs and equivalent circuit fitting showing a sharp increase in grain-boundary resistance. Complementary modulus analysis highlights strongly non-Debye relaxation with a broad distribution of relaxation times arising from cationic disorder and interfacial heterogeneity. Predominantly, La/Ce co-substitution is shown to be an effective strategy for tuning grain-boundary-controlled dielectric behavior and interfacial polarization in hard/soft ferrite nanocomposites, making these materials promising candidates for EMI shielding and high-frequency electronic applications requiring controlled impedance and reduced energy dissipation.

Keywords Hard-soft ferrites · La/Ce Co-Substitution · Conductivity · Dielectric properties · Cole-Cole analysis

✉ A. Baykal
abdulhadibaykal@aydin.edu.tr

[1] Food Engineering Department, Faculty of Engineering, Istanbul Aydin University, Florya, Istanbul 34295, Türkiye

[2] Basic Pharmacy Department, Faculty of Pharmacy, Istanbul Aydin University, Florya, Istanbul 34295, Türkiye

[3] Department of Electrical and Electronics Engineering, Faculty of Engineering and Architecture, İstanbul Gelisim University, Avcilar, Istanbul, Türkiye

[4] Department of Biophysics, Institute for Research and Medical Consultations (IRMC), Imam Abdulrahman Bin Faisal University, P.O. Box 1982, Dammam 31441, Saudi Arabia

[5] Department of Physics, College of Science, Imam Abdulrahman Bin Faisal University, P.O. Box 1982, Dammam 31441, Saudi Arabia

[6] Department of Chemistry, Istanbul Medeniyet University, Uskudar, Istanbul 34700, Türkiye

Published online: 27 February 2026

1 Introduction

The number of research about ferrite-based nanocomposites (NCs) is increasing day by day due to their magnetization, microwave absorption, unique coercivity, and electro-magnetic properties. Now these NCs are being considered as new multifunctional materials [1, 2]. The magnetic or electrical properties of them can be modified through the doing transition metal ions which will lead to the fabrication of NCs with distinct features and multifunctional applications [3]. Ferrite nanocomposites combine high coercivity of the hard phase and high magnetization of the soft phase [4]. Different spinel ferrites have been utilized in energy storage and high-frequency devices, including isolators, phase shifters, circulators, supercapacitors, miniaturized inductors/transformers, reducing energy loss in power electronics and solar cells [5–7].

Cobalt spinel ferrite ($CoFe_2O_4$ SF) is hard ferrite in comparison with other spinel counterparts. Because as compared with the other SFs, it has excellent magnetic features [8]. On the other hand, $NiFe_2O_4$ is a soft ferrite having high Ms and low values of conductivity [9]. The substitution of REs into the spinel structure leads to a distortion in the structure and introduces strains, thus altering the magnetic and electrical behaviour significantly [10]. The control of RE and/or metal ion substituents can alter electromagnetic properties of NCs by controlling different types and amounts of metal ion or substitution [11]. RE cations are likely to occupy the octahedral (B) site when they are doped into the SFs, thus, cause to enhance the electrical resistivity. Additionally, the improvement in densification, permeability, and resistivity may be obtained with doping of RE cations (La^{3+}, Ce^{3+}, Dy^{3+}, etc.) into SFs [12]. Modification in structural parameters along with magnetic behavior and electrical response of gradually RE doped SFs has been examined by many researchers.

A review of the current literature reveals that while RE ions like La^{3+} and/or Ce^{3+} have been used individually or simultaneously to modify the electrical and dielectric properties of single-phase spinel ferrites. For instance, the influence of Ce doping in magnesium ferrites has important effects on dielectric properties, and such ferrite materials have piezoelectric behavior and are being used in antenna designing [13]. Ul Haq et al. [14] studied on the influence of Ce^{3+} and La^{3+} co-doping on the structural, optical, and electrical behaviors of Mg-Zn spinel ferrites. It was observed that this co-doping leads to a significant increase in impedance and a reduction in dielectric loss. In another study, Almessiere et al. [15] established that the co-substitution of La^{3+} and Y^{3+} in Ni-Cu-Zn spinel ferrite nanoparticles results in a reduction of crystallite size caused by grain boundary pinning, which in turn increases the coercivity and microwave absorption capacity (reaching − 40 dB). The role of Ce was also emphasized in Ce substituted $Ni_{0.3}Mg_{0.5}Cu_{0.2}Fe_2O_4$ [16], where a low dielectric loss was achieved. Moreover, another study on La-substituted Mg-Co spinel ferrites [17] indicates that the large ionic radii of La^{3+} reaches a "solubility limit" at x = 0.06. The dielectric constat significantly enhanced with the introduction of La^{3+} ions.

The speedy propagation of high-frequency wireless communication and the initiation of 5G technology have significantly increased the demand for advanced functional nanomaterials that are able to operate under high-power and high-frequency settings. Spinel ferrite nanocomposites (SFNCs) are no longer just simple subjects of structural interest. Nowadays, SFNCs become crucial to mitigate electromagnetic pollution via EMI shielding and enable miniaturizing microwave devices. Nevertheless, one of the main challenges in the materials science area is the 'trade-off' amid the electrical permittivity and the magnetic loss. Accordingly, by engineering hard-soft (H/S) interfaces, such as the present studied $CoFe_2O_4/NiFe_2O_4$ system, we can accomplish a cooperative effect where the large coercivity of the H component and the great permeability of the S component are coupled to each other through controlled dielectric relaxation. Almessiere et al. [8] did research on electrical and dielectric properties of H/S NCs $CoFe_2O_4/(NiSc_{0.03}Fe_{1.97}O_4)_x$ NCs. It was confirmed that the dielectric constants of $NiSc_{0.03}Fe_{1.97}O_4$ and $CoFe_2O_4$ NPs lead to normal dielectric distribution with frequency, largely dependent on compositional ratios. In another study which was proceeded by Manner et al. [10], the magnetic and dielectric properties of Ho and Er co-substitution cobalt ferrites, were investigated and a remarkable improvement in the dielectric constant (ε′) was observed with Ho–Er substitution. Dhabekar and Kant [18] studied on the temperature dependent dielectric properties of $CoFe_2O_4$ and $SrFe_{12}O_{19}$ NCs synthesized with various weight ratios via chemical co-precipitation route, and they found out that an increase in impedance with increasing weight ratio of $SrFe_{12}O_{19}$ was observed, due to creation of effective scattering centres. Conductivity mechanism was explained by Overlappinglarge polaron tunnelling (OLPT) model. The effect of Europium on magnetic and dielectric properties of NiFe2O4 were investigated by Sivaprakash et al. [19]. The dielectric constant and loss factor decreased with the substitution of Eu^{3+}.

Although several studies investigated the properties of $CoFe_2O_4/NiFe_2O_4$ SFNCs, there is a distinct lack of studies addressing how co-substitution using two RE ions of La/Ce with different characteristics can be used to gate the electrical transport across the interface of a H/S nanocomposite. The present study fills that gap by utilizing La^{3+}

(large ionic radius) and Ce^{3+} (variable valence state) to create a synergistic effect that enhances interfacial polarization. By targeting the grain boundaries of the $CoFe_2O_4$/$NiFe_2O_4$ system, this work provides a novel approach to achieving high-frequency stability that single-ion doping cannot provide. Accordingly, we are trying in the present study to move beyond simple alteration of properties by showing how the co-substitution of rare-earth La/Ce elements acts as a precision tool for controlling the interfacial polarization, which is a key factor to optimize impedance in next-generation electronic components. To the best of our knowledge, this is the first study in which La^{3+} - Ce^{3+} ions were co-substituted into ferrite nanocomposite. In this study, the structural, electrical, and dielectric features of H/S $CoLa_xCe_xFe_{2-2x}O_4/NiFe_2O_4$ ($\leq x \leq 0.10$) SFNCs were investigated for high-frequency and thermally robust electronic applications.

Moreover, in the current situation of global energy transitions and resource management, the development of advanced multifunctional nanomaterials and nanocomposites is no longer merely a local technological endeavor, but a socio-economic requirement. Effective management of nanomaterials and the shift towards what might be called "green electronics" necessitate the design and development of components that minimize the dissipation of energy and extend working lifetime. As mentioned earlier, SFNCs can play a pivotal role in this transition. By modifying the interfacial polarization and electrical transport in hard-to-soft $CoFe_2O_4/NiFe_2O_4$ systems through the RE ions' substitution, it could be possible later to develop miniaturized inductors and transformers with considerably diminished eddy current losses. This efficiency is a key parameter for high-power electronics and renewable energy converters, as energy conservation directly impacts the economic viability of sustainable systems. Moreover, the use of the sol-gel auto-combustion method in the present study represents an effort to utilize energy-efficient synthesis routes that offer high scalability and minimal waste in comparison to conventional solid-state reactions, hence supporting circular economy models in materials manufacturing. The sol–gel auto-combustion process serves as a self-sustaining technique for generating heat through its exothermic reactions, providing several advantageous characteristics such as uniformity, reduced particle size, improved distribution, and controlled morphology. Sol–gel auto-combustion is a fast and cost-effective synthesis method for the construction of particulate materials. It has been extensively used to synthesize different nanoparticles, creating nano-sized, uniform, and highly reactive powders by combining elements at the atomic level [20]. Sol-gel auto-combustion is a self-sustaining process that generates heat through its exothermic reaction [21].

2 Experimental

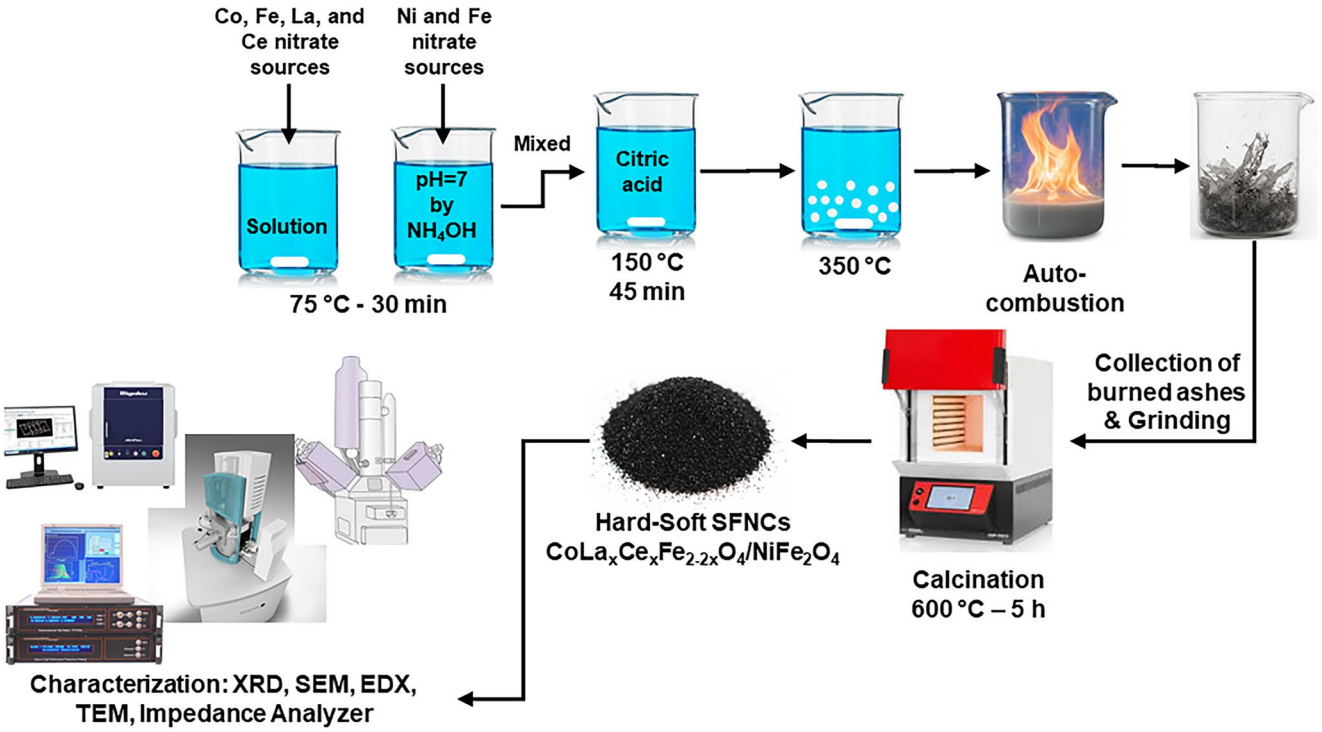
All precursors (high grade) were taken from Merck ($Co(NO_3)_2.3H_2O$ (99.9%), $Ni(NO_3)_2.6H_2O$ (≤98.5%), $Fe(NO_3)_3.9H_2O$ (≤98.5%), $La(NO_3)_3.6H_2O$ (≤98.5%), $Ce(NO_3)_3.6H_2O$ (≤99%), NH_4OH (25%) and urea (CH_4N_2O) (≤98%).

The crystal structure of all products was analyzed using Rigaku Miniflex 600 X-ray powder diffractometer (λ_{Cu}). SEM (Tescan Vega 3) coupled with EDX spectrometer, TEM, and HR-TEM (JEOL) microscopies were used for morphology and chemical composition analysis. The electrical conductivity and and dielectric measurements of all samples were studied in the temperature range of 20–120 °C with a heating rate of 10 °C/s. The sample was used in the form of circular pellets of 13 mm diameter and 3 mm thickness. The pellets (both nanocomposite and pristine) were sandwiched between gold electrodes, and the conductivities were measured using Novocontrol dielectric impedance analyzer in the frequency range of 0–3 MHz, respectively. The temperature (between 100 and 250 °C) was controlled with a Novocool Cryosystem.

Stoichiometric amounts of metal salts were dissolved in deionized H_2O to prepare two solutions of $CoLa_xCe_xFe_{2-2x}O_4$ as hard and $NiFe_2O_4$ as soft, separately. The x in the chemical formula of the hard phase represents the molar concentration of La^{3+} and Ce^{3+} ions individually. For each composition ($x = 0.00$, 0.02, 0.04, 0.06, 0.08, and 0.10), the total trivalent rare-earth content is $2x$, substituting an equivalent $2x$ amount of Fe^{3+} cations. Once completely dissolved, the hard and soft solutions, in a 1:1 ratio, were mixed along with a certain amount of citric acid by stirring at 75 °C for 30 min. After adjusting the pH of the solution to 7 with NH_4OH, it was heated up at 150 °C for 45 min. Then the temperature was raised to 350 °C for the generation of viscous gels. At the end of this heating process, the viscous gel was burned to get black powder. Finally, the obtained solid product was calcinated at 600 °C for 5 h [22]. The different experimental steps are illustrated in Scheme 1.

2.1 Experimental uncertainties

Experimental uncertainties originate from precursor purity, synthesis conditions, sample preparation, and instrumental constraints. Although high-purity reagents were employed, minor compositional fluctuations and local inhomogeneities may arise during the sol–gel process and subsequent calcination, particularly at higher La/Ce substitution levels. Pellet preparation (variations in thickness, surface flatness, and electrode–sample contact) can also introduce uncertainty in the absolute values of conductivity and permittivity, despite



Scheme 1 Synthesis phases and characterization of H/S $CoLa_xCe_xFe_{2-2x}O_4/NiFe_2O_4$ ($x \leq 0.10$) SFNCs

maintaining identical pressing conditions and using gold electrodes for all measurements. In addition, the Novocontrol dielectric impedance analyzer exhibits increased noise at the lowest and highest frequency limits, which may affect data accuracy; therefore, quantitative analyses were confined to frequency regions with reliable signal-to-noise ratios. Equivalent electrical circuit fitting further introduces uncertainty due to parameter correlation and non-uniqueness of solutions.

2.2 Reliability considerations

Data reliability was ensured by repeating the synthesis and electrical measurements under identical conditions, yielding consistent trends within experimental error. Physically meaningful equivalent circuit models, supported by structural and microstructural characterization, were employed to minimize ambiguity in fitting results, and fitting quality was evaluated using standard error metrics. The convergence of conclusions drawn from impedance, modulus, and dielectric analyses provides cross-validation of the observed transport and polarization mechanisms. Overall, while acknowledging the inherent uncertainties associated with broadband dielectric spectroscopy of NC ferrites, the reproducibility of the results and the consistency across multiple analytical approaches support the robustness and reliability of the reported findings.

3 Results & discussion

3.1 Structure & morphology

XRD powder patterns of $CoLa_xCe_xFe_{2-2x}O_4/NiFe_2O_4$ ($x \leq 0.10$) SFNCs were depicted in Fig. 1. A single XRD pattern for all compositions (except for $x = 0.08$ and 0.1 samples for which minor amount of α-Fe_2O_3 and CeO_2 were observed) which belongs to the cubic crystal lattice with the F*d*3*m* space group. Miller indices (220), (311), (222), (400), (331), (422), (511), (440), (620), (533), and (622) were assigned for ICDD card #00–001−1121 ($CoFe_2O_4$). The single phase at lower co-substitution concentrations also indicated that the addition of La^{3+}/Ce^{3+} ions was well tolerated by the host lattice ions, keeping the cubic symmetry of H/S $CoLa_xCe_xFe_{2-2x}O_4/NiFe_2O_4$ ($x \leq 0.10$) SFNCs [23]. The detection of secondary peaks at higher x values indicates that the solubility limit of RE ions within the cubic spinel lattice has been reached. This restricted dopability is expected, as the large RE cations create excessive lattice distortion, which favor the formation of secondary phases (such as α-Fe_2O_3 and CeO_2) at the grain boundaries rather than further substitution into the desired Fe sites.

The crystallite size (D_{XRD}) of the products was estimated using Scherrer equation considering the (311) peak and was found to be within 26 to 43 nm (Table 1). As shown in Table 1, the crystallite size systematically diminishes as the

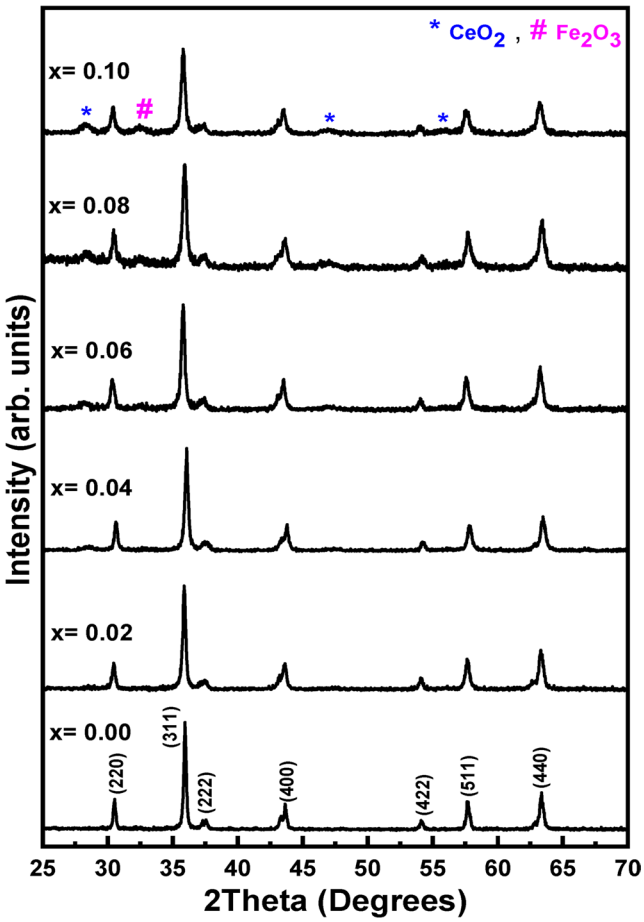


Fig. 1 XRD powder patterns of H/S $CoLa_xCe_xFe_{2-2x}O_4/NiFe_2O_4$ ($x \leq 0.10$) SFNCs. The * and # symbols represent the secondary phases α-Fe_2O_3 and CeO_2, respectively

La/Ce concentration increases within the H/S SFNC. The intensity of the reflection peaks in the XRD pattern decreases with co-substitution, suggesting a reduction in crystallinity and the difficulty in incorporating La and Ce into the spinel lattice. Several variables affect the intensity of each peak, including the size of the crystals, the molecular composition of each sample, the X-ray voltage of the machine, the step scan, and the duration of the scan during which the diffraction patterns were obtained, as well as the measured diffraction planes. Each factor influences the product's intensity and crystallinity. The crystallite size decreases because of the mismatch in ionic radii between RE ions (r_{La3+} = 1.03 Å, r_{Ce3+} = 1.01 Å) and Fe^{3+} ions (r_{Fe} = 0.64 Å) would introduce structural distortions and lattice strain [24]. Moreover, because of their large size, RE ions exhibit low solubility in the spinel lattice and tend to segregate at the grain boundaries. This segregation implies a pinning effect that hinders the migration of grain boundaries during the heating process, consequently restricting grain growth and promoting the reduction of crystallite size. Similar trends of reduction in D_{XRD} have been reported in other Ho/Dy, Ce/Sm, and Sm/Er co-substituted spinel ferrites [25, 26]. Er and Dy substitution in cobalt spinel ferrites also showed a similar trend [27]. This highlights the influence of RE ions in hindering the crystallite growth and promoting the reduction of crystallite size.

SEM was used to examine the surface morphology of the as-prepared H/S $CoLa_xCe_xFe_{2-2x}O_4/NiFe_2O_4$ (x = 0.00, 0.04 and 0.08) SFNCs, as illustrated in Fig. 2(a). The SEM images indicated the presence of small nanoparticles exhibiting condensed agglomeration of spherical particles. Additionally, it was noted that during burn-off, there are certain pores or cavities as a result of disintegration and the gel-to-solid transition. The chemical composition of the synthesized H/S $CoLa_xCe_xFe_{2-2x}O_4/NiFe_2O_4$ (x = 0.04 and 0.08) was analyzed using EDX, as illustrated in the figure. Figure 2(b) illustrates the EDX spectra of the H/S SFNCs. EDX analysis identified the presence of Ni, Co, Ce, La, Fe, and O. The results confirmed the successful synthesis of the composites. The structural design of H/S $CoLa_xCe_xFe_{2-2x}O_4/NiFe_2O_4$ (x = 0.06) SFNCs was validated through TEM and HR-TEM analysis, as illustrated in Fig. 3. TEM effectively reveals spherical particles. The HR-TEM image displays organized lattice fringes associated with H/S SFNCs, with interplanar distances computed using GATAN software.

3.2 Electrical spectroscopy

This work addresses fundamental condensed-matter questions regarding how ionic doping, lattice disorder, and electronic transport are interrelated in mixed-valence spinel oxides. The results demonstrate that aliovalent substitution in spinel ferrites does not produce a monotonic enhancement of electrical or dielectric properties; rather, it establishes a competition between defect-assisted carrier generation and

Table 1 Crystallography parameters of H/S $CoLa_xCe_xFe_{2-2x}O_4/NiFe_2O_4$ ($x \leq 0.10$) SFNCs. a_o: lattice constant; crystallite size (D_{XRD} (nm)):, L(A) and L(B) (in nm): hopping lengths for site A and B, respectively

x	a_o (Å)	V $(Å)^3$	D_{XRD} (nm)	Microstrain (ε) $x10^{-3}$	L(A)	L(B)
0.00	8.299	571.545	43.44	2.703	3.593	2.934
0.02	8.276	566.853	34.72	3.368	3.584	2.926
0.04	8.285	568.605	31.90	3.669	3.587	2.929
0.06	8.305	572.727	30.78	3.830	3.596	2.936
0.08	8.314	574.844	26.11	4.514	3.600	2.939
0.10	8.328	577.749	27.61	4.269	3.606	2.945

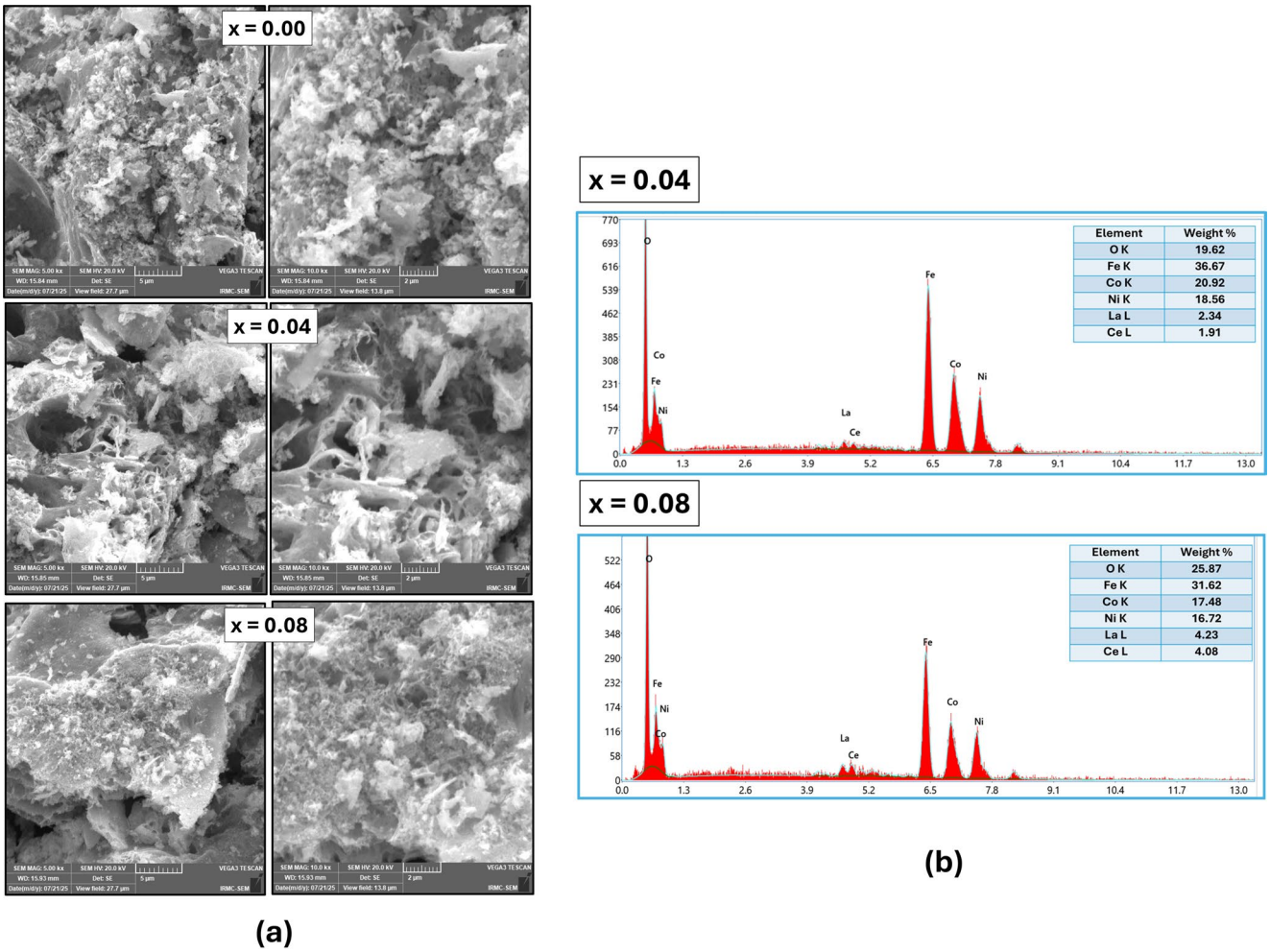


Fig. 2 (**a**) SEM images of H/S $CoLa_xCe_xFe_{2-2x}O_4/NiFe_2O_4$ SFNCs (x = 0.00, 0.04, and 0.08) and (**b**) EDX spectra of H/S $CoLa_xCe_xFe_{2-2x}O_4/NiFe_2O_4$ (x = 0.04 and 0.08) SFNCs

disorder-induced carrier localization. At low dopant concentrations, local lattice distortions and isolated defect states act as carrier traps, increasing activation energy, whereas at intermediate concentrations an optimal regime emerges in which a balanced Fe^{2+}/Fe^{3+} mixed-valence state, partial lattice relaxation, and controlled defect distribution enable percolative small-polaron hopping with minimized transport barriers. At high dopant levels, excessive disorder, defect clustering, and secondary phase formation drive the system into an interface-controlled regime where grain boundaries and phase interfaces dominate charge transport and give rise to pronounced MW polarization. This behavior establishes a general principle for doped spinel systems: functional optimization occurs within a narrow defect-percolation window, beyond which structural and electronic disorder negate the benefits of increased carrier density. These conclusions are strongly supported by recent physics-informed and data-driven studies showing that lattice parameters in spinel oxides are quantitatively governed by ionic radii, electronegativity, and site occupancy [28, 29], providing a robust basis for attributing the observed lattice distortions to substitution-induced strain and site disorder. Moreover, statistical modeling of transport in complex oxides highlights that defect populations, compositional heterogeneity, and microstructural complexity generate distributed conduction pathways [30–32], consistent with the non-Debye relaxation and broadened ImM response observed here. Analogous synthesis–property correlations reported for magnetic and oxide systems further confirm that subtle compositional variations can induce highly non-linear functional responses [31, 32]. Collectively, these findings situate the present results within contemporary defect- and interface-engineering frameworks and underscore the central role of microstructural heterogeneity and interfacial physics in governing transport and polarization in spinel ferrites and related functional oxides.

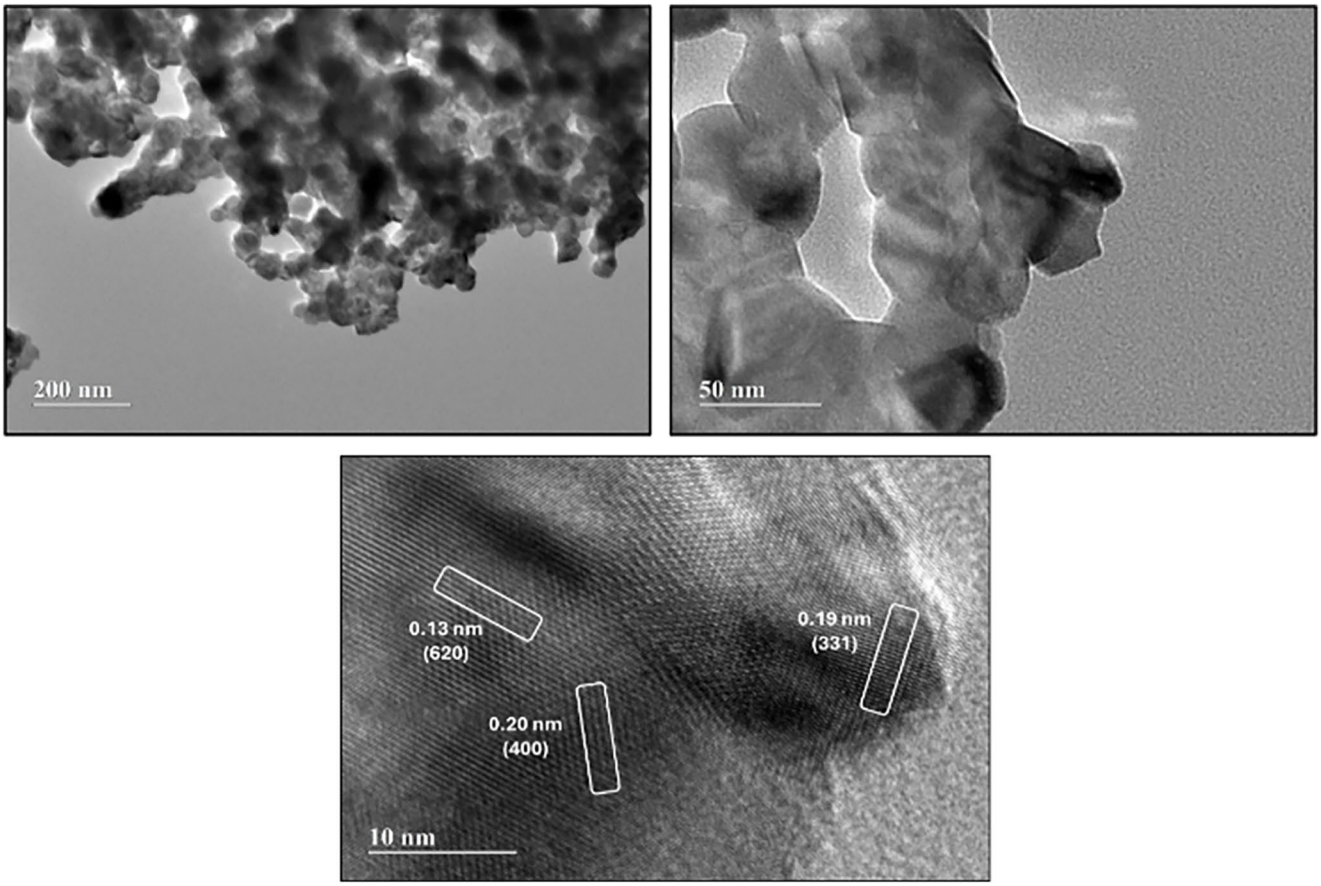


Fig. 3 TEM (upper images) and HR-TEM (lower images) images of H/S $CoLa_{0.06}Ce_{0.06}Fe_{1.88}O_4/NiFe_2O_4$ (x = 0.06) SFNCs

3.2.1 AC conductivity (3D) analysis

Figure 4 presents 3D surface plots illustrating the dependence of AC conductivity, expressed as *ln(σ)* (*S/cm*), on logarithmic frequency (*ln[f(Hz)*]) and temperature (°C) for H/S $CoLa_xCe_xFe_{2-2x}O_4/NiFe_2O_4$ SFNCs with substitution levels ranging from x = 0.00 to 0.10. These plots provide a comprehensive representation of how electrical conductivity evolves as a function of both composition and thermal activation.

For the undoped and lightly substituted samples (x = 0.00, 0.02, and 0.04), the AC conductivity increases gradually with both frequency and temperature. In the low-frequency region, the conductivity remains relatively constant at lower temperatures and becomes more frequency dependent as the temperature increases. This behavior is indicative of a thermally activated conduction process and is consistent with small-polaron hopping. Moreover, the smooth and nearly monotonic variation of conductivity with frequency suggests a relatively uniform transport mechanism, in which grain-boundary contributions dominate the overall conduction response [19, 33].

At intermediate substitution levels (x = 0.06–0.08), the conductivity surfaces exhibit enhanced curvature and stronger temperature sensitivity, particularly at low frequencies. In this range, the conductivity increases more rapidly with temperature, reflecting improved charge-carrier mobility. This enhancement can be attributed to an optimal balance between La/Ce incorporation and Fe-site occupancy, which reduces localized trapping effects and facilitates hopping transport. Consequently, these compositions likely exhibit mixed conduction behavior, with significant contributions from both grain interiors and grain boundaries.

In contrast, at the highest substitution level (x = 0.10), the conductivity surface becomes highly irregular, especially at low temperatures and frequencies. Such behavior indicates a disruption of continuous conduction pathways due to excessive dopant-induced lattice distortion and structural disorder. The presence of non-monotonic trends and abrupt changes in conductivity suggests increased charge localization and possible phase inhomogeneity, which are commonly associated with defect clustering and enhanced scattering of charge carriers [19, 34].

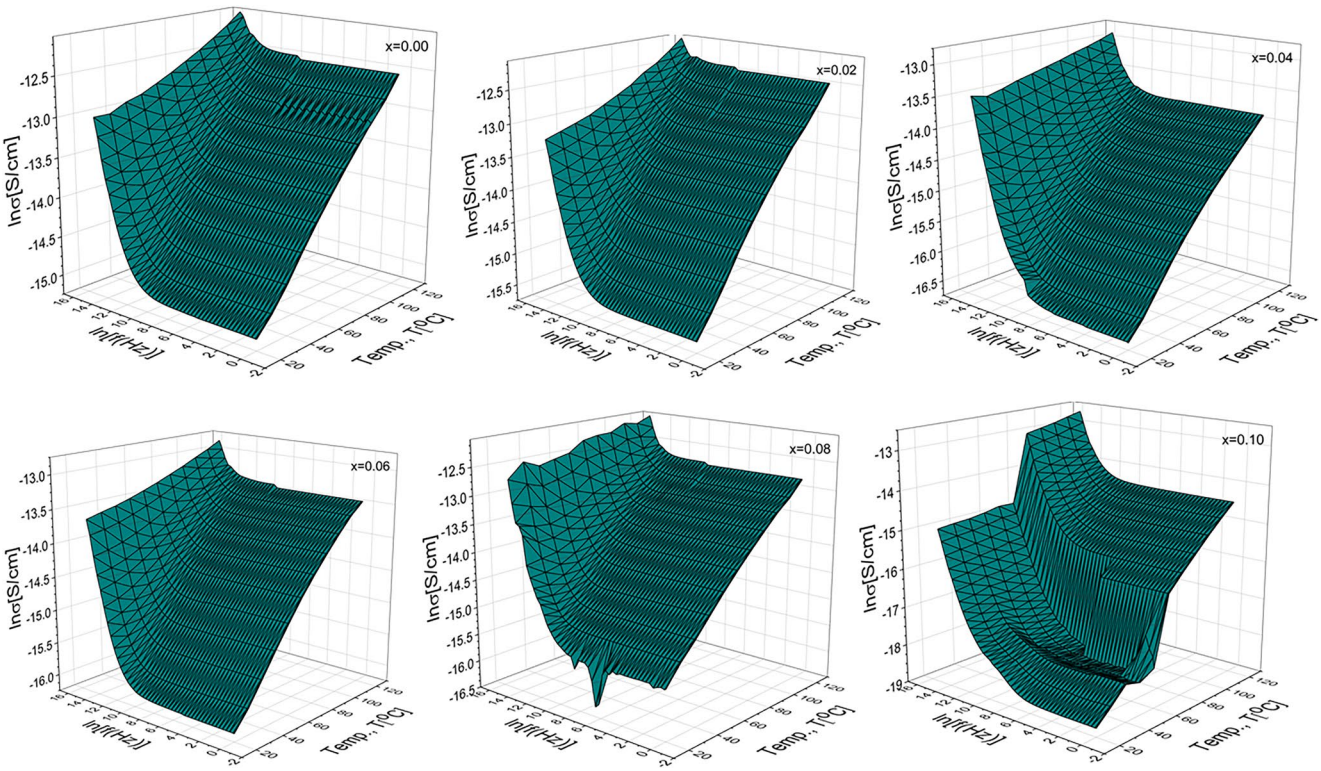


Fig. 4 3D representation of AC Conductivity of H/S $CoLa_xCe_xFe_{2-2x}O_4/NiFe_2O_4$ ($x \leq 0.10$) SFNCs

Across all compositions, the overall increase in AC conductivity with both frequency and temperature confirms the thermally activated nature of the conduction mechanism. At low frequencies, charge carriers tend to accumulate at grain boundaries, leading to lower conductivity. However, as the frequency increases, carriers can more effectively follow the alternating electric field, thereby contributing to higher conductivity. La/Ce co-substitution initially enhances electrical conductivity, particularly for $x \approx 0.06$–0.08, due to improved charge delocalization. Nevertheless, further substitution beyond this range results in degraded electrical performance as disorder and carrier localization become dominant [19, 34].

To further elucidate the conduction mechanism, the AC conductivity spectra were analyzed using Jonscher's universal power law, $\sigma(\omega, T) = \sigma_{dc}(T) + A(T)\omega^{s(T)}$, where the frequency exponent *s(T)* provides direct insight into the dominant charge-transport process and angular frequency $\omega = 2\pi f$. The values of *s(T)* were extracted from the slope of the linear region of $\ln\sigma_{ac}$ versus ln(ω) at fixed temperatures, focusing on the high-frequency dispersive regime of the conductivity spectra (Table 2). For all compositions, *s(T)* decreases monotonically with increasing temperature, as reflected by the progressive flattening of the conductivity surfaces at elevated temperatures.

Table 2 Frequency exponent *s*(*T*) extracted from the slope of the dispersive region in Fig. 4

x	*s*(30 °C)	*s*(60 °C)	*s*(90 °C)	*s*(120 °C)	Dominant mechanism
0.00	0.78	0.70	0.62	0.56	CBH
0.02	0.76	0.68	0.60	0.54	CBH
0.04	0.73	0.65	0.58	0.52	CBH
0.06	0.68	0.58	0.50	0.44	CBH → SPH
0.08	0.60	0.48	0.40	0.35	SPH
0.10	0.55	0.45	0.36	0.30	SPH

For samples with low La/Ce substitution levels ($x \leq 0.04$), the exponent *s(T)* decreases moderately with temperature and remains within the range of approximately 0.5–0.8. This behavior is characteristic of the correlated barrier hopping (CBH) mechanism. As the substitution level increases to $x = 0.06$, *s(T)* exhibits a stronger temperature dependence, indicating enhanced carrier localization and suggesting a gradual transition from CBH to small-polaron hopping (SPH). At higher substitution levels ($x = 0.08$ and 0.10), *s(T)* decreases more rapidly with temperature and reaches values below 0.4 at elevated temperatures, confirming that SPH becomes the dominant conduction mechanism, particularly across grain boundaries and interfacial regions.

Furthermore, the absence of temperature-independent *s(T)* values excludes quantum mechanical tunneling as the

primary transport mechanism, while the lack of an increasing *s(T)* trend with temperature rules out non-overlapping small-polaron tunneling. Overall, the systematic evolution of *s(T)* with composition reflects the increasing influence of lattice distortion, defect-induced disorder, and interfacial heterogeneity introduced by La/Ce co-substitution. Accordingly, charge transport in the H/S SFNCs evolves from CBH-dominated conduction at low substitution levels to SPH-controlled transport at higher substitution levels, in good agreement with the dielectric relaxation, impedance, and electric modulus analyses presented elsewhere in this work.

In conclusion, the 3D AC conductivity profiles of H/S $CoLa_xCe_xFe_{2-2x}O_4/NiFe_2O_4$ SFNCs demonstrate a strong interdependence of substitution ratio, temperature, and frequency on conduction dynamics. Moderate co-substitution levels ($x \approx 0.06$–0.08) optimize charge transport by promoting thermally assisted hopping mechanisms, whereas excessive substitution ($x = 0.10$) introduces significant structural disorder that hinders electronic mobility. These findings highlight the effectiveness of controlled La/Ce co-substitution in tuning the electrical properties of H/S SFNCs for high-frequency and thermally stable electronic applications.

3.2.2 AC and DC Conductivity Analysis

The electrical transport behavior of H/S $CoLa_xCe_xFe_{2-2x}O_4/NiFe_2O_4$ ($x \leq 0.10$) SFNCs was investigated through combined AC(2D) and DC conductivity analyses, as presented in Fig. 5. Together, these results reveal that charge transport in the system is governed by thermally activated hopping mechanisms that are strongly influenced by La/Ce substitution and microstructural heterogeneity.

Figure 5(a) illustrates the frequency dependence of AC conductivity for the representative composition $x = 0.06$ over the temperature range of 20–120 °C. At low frequencies, the conductivity exhibits a nearly frequency-independent plateau corresponding to the DC conductivity (σ_{dc}), indicating long-range charge transport. As the frequency increases, a dispersive region appears in which the conductivity increases monotonically with frequency. This behavior is characteristic of hopping conduction in disordered ferrite systems and is well described by Jonscher's universal power law. Moreover, the onset frequency of dispersion shifts toward higher frequencies with increasing temperature, which reflects a reduction in relaxation time and enhanced charge-carrier mobility due to thermal activation. This confirms that AC conduction is dominated by thermally assisted hopping processes, particularly across grain boundaries and interfacial regions.

The DC conductivity behavior is further clarified by the Arrhenius plots of $\ln\sigma_{dc}$ versus $1/k_BT$ shown in Fig. 5(b). For all compositions, the approximately linear dependence indicates thermally activated conduction governed by an Arrhenius-type mechanism, commonly associated with small-polaron hopping between localized Fe^{2+} and Fe^{3+} ions. The undoped sample exhibits the steepest Arrhenius slope, corresponding to the highest activation energy (E_a), which suggests a relatively large barrier for charge hopping due to limited defect-assisted pathways and dominant grain-boundary resistance [19, 35, 36].

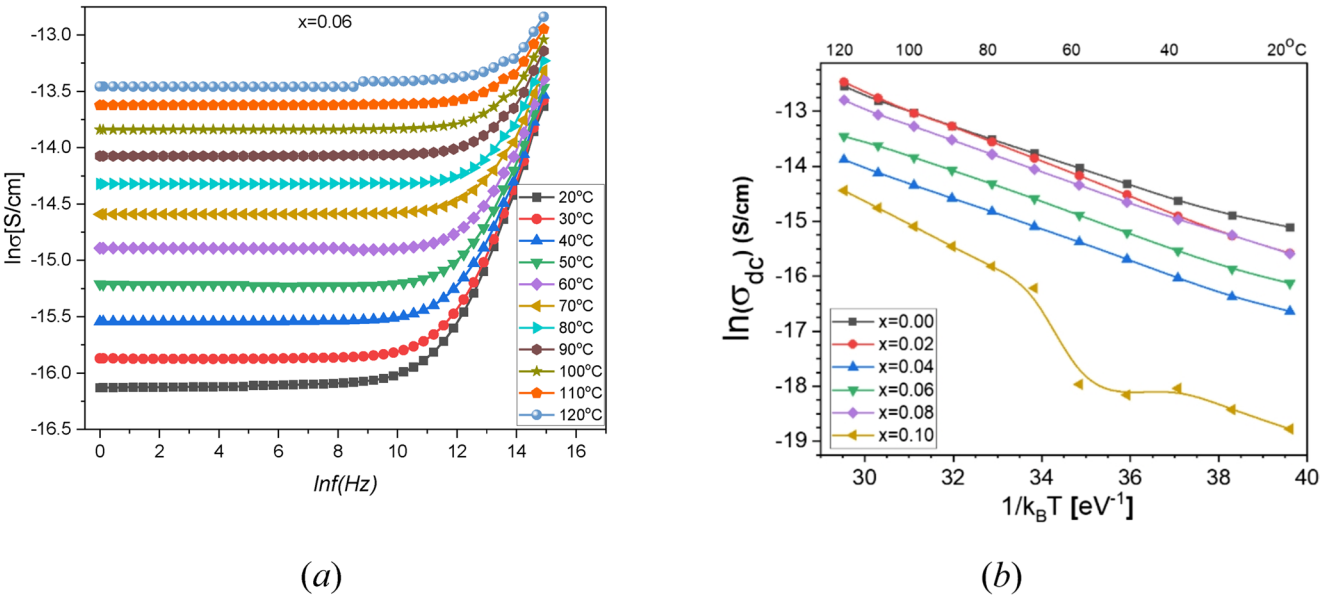


Fig. 5 2D representation of *ac* conductivity ($x = 0.06$) and Arrhenius plot of the *dc* conductivity of H/S $CoLa_xCe_xFe_{2-2x}O_4@NiFe_2O_4$ ($x \leq 0.10$) SFNCs

With initial La/Ce substitution (x = 0.02–0.06), the activation energy decreases, as evidenced by the shallower slopes of the Arrhenius plots. This reduction in E a arises from the incorporation of La^{3+} and Ce^{4+} ions into the spinel lattice, which modifies the Fe^{2+}/Fe^{3+} ratio and introduces localized defect states. Consequently, the probability of small-polaron hopping increases, leading to enhanced charge delocalization and improved DC conductivity. In this substitution range, defect-assisted hopping effectively facilitates both DC transport and the high-frequency AC response [19, 33, 37].

At higher substitution levels, particularly at x = 0.08, the Arrhenius behavior remains thermally activated but begins to show slight deviations at elevated temperatures. This indicates a transitional regime in which the beneficial effects of substitution-induced defects start to compete with disorder-related scattering mechanisms. In this regime, conduction through relatively conductive grain interiors coexists with increasingly resistive grain-boundary and interfacial pathways, as also reflected in the AC conductivity dispersion.

For the highest substitution level (x = 0.10), the Arrhenius plot exhibits a significantly steeper slope, especially at lower temperatures, indicating a renewed increase in activation energy. This behavior reflects the detrimental effects of excessive doping, including severe lattice distortion, defect clustering, and the formation of deep trap states. These factors disrupt continuous hopping pathways and promote strong carrier localization, leading to reduced DC conductivity despite higher dopant concentration. Correspondingly, AC conduction becomes increasingly dominated by localized hopping and interfacial polarization effects rather than long-range transport [35, 37].

Overall, the combined AC and DC conductivity analyses demonstrate that charge transport in H/S $CoLa_xCe_xFe_{2-2x}O_4/NiFe_2O_4$ (x ≤ 0.10) SFNCs is governed by thermally activated hopping mechanisms. Moderate La/Ce substitution optimizes defect-assisted conduction and enhances carrier mobility, whereas excessive substitution introduces structural disorder and interfacial barriers that suppress conductivity. The strong consistency between the frequency-dependent AC response and Arrhenius-type DC behavior provides a unified understanding of the transport processes and confirms the critical role of controlled doping in tailoring the electrical properties of hard–soft ferrite nanocomposites [19, 35, 36].

3.2.3 Activation energy analysis

Table 3 summarizes the extracted E_a for the *dc* conductivity of H/S $CoLa_xCe_xFe_{2-2x}O_4/NiFe_2O_4$ (x ≤ 0.10) SFNCs. The E_a `s were calculated from the slope of the Arrhenius plots ($ln\sigma$ vs. $1/k_BT$) assuming a thermally activated small polaron hopping mechanism [36, 38, 39].

The unsubstituted sample ($x = 0.00$) shows an E_a of 0.258 eV, reflecting the intrinsic conduction barrier of the base $NiFe_2O_4$ system. This relatively moderate value is consistent with polaron hopping between Fe^{2+} and Fe^{3+} ions in a well-ordered spinel lattice.

A slight increase in substitutions to $x = 0.02$ leads to an increase in the magnitude of the E_a (0.311 eV). This rise suggests that the initial incorporation of *La* and *Ce* may disrupt the lattice periodicity, introducing localized defect states that act as traps, thereby increasing the energy barrier for hopping conduction.

At intermediate substitution levels ($x = 0.04$ and 0.06), the E_a `s stabilize around 0.275 to 0.278 eV. This relative flattening of E_a values indicates that moderate doping levels optimize the balance between defect-assisted conduction pathways and structural disorder. Similar E_a values suggest that the hopping mechanism is maintained with minimal additional trap states or blocking effects, allowing for efficient electron transport between *Fe* sites [19, 35, 36, 38, 39].

For $x = 0.08$, the E_a remains comparable (0.277 eV), suggesting that up to this level, the spinel lattice can accommodate the substitution ions without significantly increasing carrier trapping or disrupting polaron hopping pathways. This stability may be associated with a saturation of favourable defect states facilitating conduction.

A dramatic increase in the magnitude of the E_a is observed at $x = 0.10$ (0.474 ± 0.043 eV), indicating a significant reduction in electrical conductivity. This large rise in E_a reflects severe lattice distortion and clustering of dopant ions, which can introduce deep trap states and hinder the continuity of hopping pathways. Such effects are typical in heavily-doped spinel's where excessive substitution disrupts the cation distribution and local electronic structure.

Overall, the data show an optimal doping window ($x \approx 0.04$–0.08) where E_a `s are relatively low and stable, supporting efficient polaron hopping. Outside this range, particularly at the highest doping level, conduction is strongly suppressed due to increased structural disorder [19, 33, 36, 39, 40].

Table 3 E_a values of H/S $CoLa_xCe_xFe_{2-2x}O_4/NiFe_2O_4$ (x ≤ 0.10) SFNCs

x	0.00	0.02	0.04	0.06	0.08	0.10
Ea (eV)	0.258	0.311	0.278	0.275	0.277	0.474

3.3 Dielectric spectroscopy

Dielectric spectroscopy is a powerful tool for elucidating charge transport, polarization, and relaxation phenomena in complex oxide systems, as it probes the frequency- and temperature-dependent response of charge carriers and dipoles under an alternating electric field. In heterogeneous ferrite-based nanocomposites, such as H/S $CoLa_xCe_xFe_{2-2x}O_4/NiFe_2O_4$ ($x \leq 0.10$) SFNCs, dielectric behavior is governed by the interplay between grain interiors, grain boundaries, and interfacial regions, all of which are strongly influenced by cation substitution and thermal activation.

In this section, the dielectric response of La/Ce co-substituted H/S $CoFe_2O_4/NiFe_2O_4$ SFNCs is systematically investigated over a broad range of frequencies and temperatures. The analysis focuses on key dielectric parameters, including the real and imaginary parts of the permittivity, dielectric loss, impedance, and electric modulus, in order to clarify the underlying conduction and relaxation mechanisms. Particular attention is given to the evolution of Maxwell–Wagner polarization, non-Debye relaxation behavior, and the transition from grain-dominated to grain-boundary/interface-controlled transport induced by increasing La/Ce content and temperature.

3.3.1 Dielectric constant analysis

Figure 6 displays a series of six 3D plots, each illustrating the dielectric constant of a composite material, H/S $CoLa_xCe_xFe_{2-2x}O_4/NiFe_2O_4$ ($x \leq 0.10$) SFNCs as a function of both frequency (in Hz) and temperature (in ^oC). The substitution ratio '*x*' varies from 0.00 to 0.10, with specific values of x = 0.00, 0.02, 0.04, 0.06, 0.08 and 0.10 presented in separate subplots. The vertical axis in each plot represents $\ln(\epsilon')$, which is the natural logarithm of the dielectric constant. From an academic perspective, this figure aims to elucidate the complex interplay between composition (specifically the *La* and *Ce* substitution ratio '*x*'), frequency, and temperature on the dielectric properties of the H/S $CoLa_xCe_xFe_{2-2x}O_4/NiFe_2O_4$ ($x \leq 0.10$) SFNCs. By comparing the plots for different '*x*' values, one can analyze how the incorporation of *La* and *Ce* (replacing *Fe* in the cobalt ferrite part of the composite) affects the overall dielectric response. Changes in the magnitude and peak positions of $\ln(\epsilon')$ across different '*x*' values would indicate the impact of these substitutions on the material's polarization mechanisms. For instance, the general trend appears to show that with increasing *x*, the dielectric constant exhibits a notable peak, particularly at lower frequencies and certain temperature ranges [19, 33, 41].

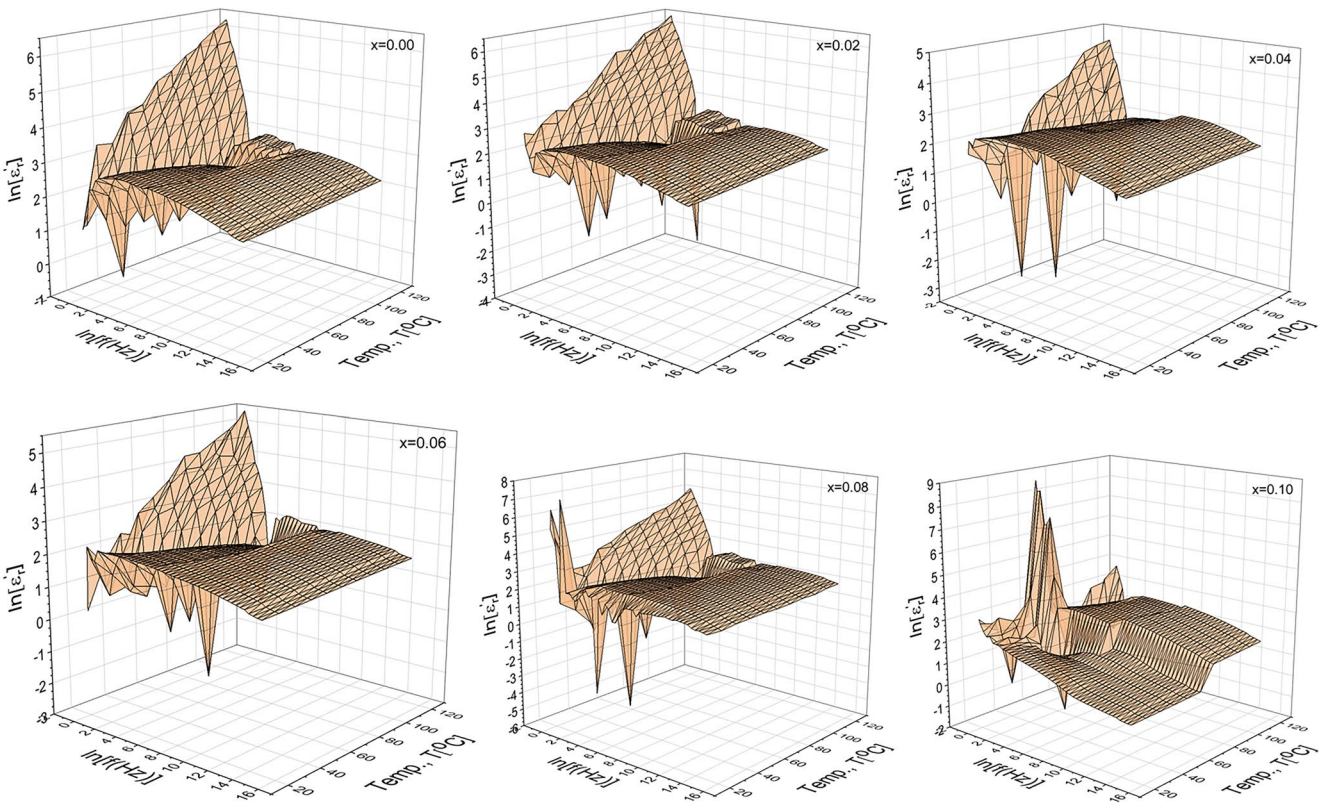


Fig. 6 3D representation of dielectric constant of H/S $CoLa_xCe_xFe_{2-2x}O_4/NiFe_2O_4$ ($x \leq 0.10$) SFNCs

The plots in the relevant figure clearly show the frequency dispersion of the dielectric constant. Typically, dielectric materials exhibit higher dielectric constants at lower frequencies due to the ability of various polarization mechanisms (interfacial, dipolar, ionic) to respond to the applied electric field. As the frequency increases, some of these mechanisms may lag, leading to a decrease in the dielectric constant. The 3D representation allows for a visualization of this dispersion across the entire temperature range.

The variations in ln(ϵ′) with temperature are also evident. Dielectric constant often shows a temperature dependence, which can be related to phenomena like phase transitions, relaxation processes (e.g., hopping of charge carriers, reorientation of dipoles), or changes in charge carrier mobility. The presence of peaks or distinct features at specific temperatures suggests the occurrence of such processes. For example, some plots show an increase in dielectric constant with temperature, potentially indicating thermally-activated hopping or increased molecular mobility.

The pronounced peaks observed in certain plots, particularly at higher values of x (e.g., $x=0.10$), are of significant interest. These anomalies are typically associated with two primary mechanisms: (i) *Relaxation phenomena*, which can be attributed to the reorientation of dipoles or the hopping of charge carriers between localized sites. Such relaxation processes commonly exhibit a frequency-dependent shift in peak position, consistent with Arrhenius-type behaviour [19, 36, 39]. (ii) *Maxwell–Wagner (MW) interfacial polarization*, which is prevalent in heterogeneous systems, such as composites or granular materials. In these systems, charge carriers tend to accumulate at the interfaces between distinct phases or at grain boundaries, leading to elevated apparent dielectric constants, particularly at lower frequencies. The pronounced rise in dielectric response at low frequencies, observed in several plots and especially for larger x values, is a characteristic feature of MW polarization [42–45].

The study of H/S $CoLa_xCe_xFe_{2-2x}O_4/NiFe_2O_4$ ($x\leq0.10$) SFNCs implies a core-shell or similar composite structure. The dielectric properties of such composites are a convolution of the properties of the individual components and the nature of their interface. The substitutions in the cobalt ferrite component are expected to influence the charge carrier concentration, mobility, and magnetic properties, which, in turn, can affect the dielectric behaviour of the entire composite.

In conclusion, the three-dimensional representation offers a comprehensive visualization of the dielectric behaviour of the H/S $CoLa_xCe_xFe_{2-2x}O_4/NiFe_2O_4$ ($x\leq0.10$) SFNCs, effectively illustrating the combined influence of compositional variation, frequency, and temperature. A more detailed academic investigation would entail the extraction and quantitative analysis of key parameters from these plots, such as peak positions, magnitudes, and relaxation frequencies, in order to elucidate the fundamental physical mechanisms governing the observed dielectric response. These mechanisms may include charge carrier hopping, interfacial MW polarization, as well as ferroelectric or relaxor ferroelectric behaviour [36, 38, 39, 46].

3.3.2 Dielectric Loss Analysis

Figure 7 presents six three-dimensional surface plots depicting the dielectric loss (ε″) of H/S $CoLa_xCe_xFe_{2-2x}O_4/NiFe_2O_4$ ($x\leq0.10$) SFNCs as a function of frequency and temperature. The dielectric loss axis is plotted as ln(ε″) in order to clearly resolve variations over a broad dynamic range. These representations offer a detailed view of how energy dissipation evolves with rare-earth co-substitution, thermal activation, and the frequency of the applied AC electric field.

Dielectric loss (ε″) quantifies the portion of electrical energy converted into heat under an alternating field and arises from multiple contributions, including charge transport losses, dipolar and interfacial polarization, and defect-assisted relaxation processes. A comparative examination of the 3D surfaces indicates that La/Ce co-substitution significantly alters the dissipation landscape. For compositions with $x\leq0.08$, the ε″ surfaces remain relatively smooth and continuous, implying a more uniform loss mechanism. In contrast, a clear modification of surface morphology is observed at $x=0.10$, pointing to the onset of additional or competing loss processes at higher substitution levels.

For all compositions, ε″ shows a pronounced dependence on frequency, with a systematic decrease as frequency increases, particularly in the low-frequency regime. This behavior is typical of ferrite-based dielectric systems in which DC conductivity and space-charge polarization dominate at low frequencies, where charge carriers can migrate and accumulate at grain boundaries, interfaces, or defect sites. At higher frequencies, these carriers are unable to follow the rapidly oscillating electric field, resulting in a reduced contribution to dielectric loss, in agreement with established dielectric models for oxide semiconductors and ferrites [36–39].

The temperature dependence of ε″ provides further insight into the governing dissipation mechanisms. As temperature increases, thermally activated charge carriers exhibit enhanced mobility, which increases electrical conductivity and, consequently, dielectric loss, particularly at low frequencies. In addition, the appearance of humps or peaks in ε″—either with increasing temperature at fixed frequency or with varying frequency at fixed temperature—signifies dielectric relaxation phenomena. Such features arise when the characteristic relaxation time of dipoles or

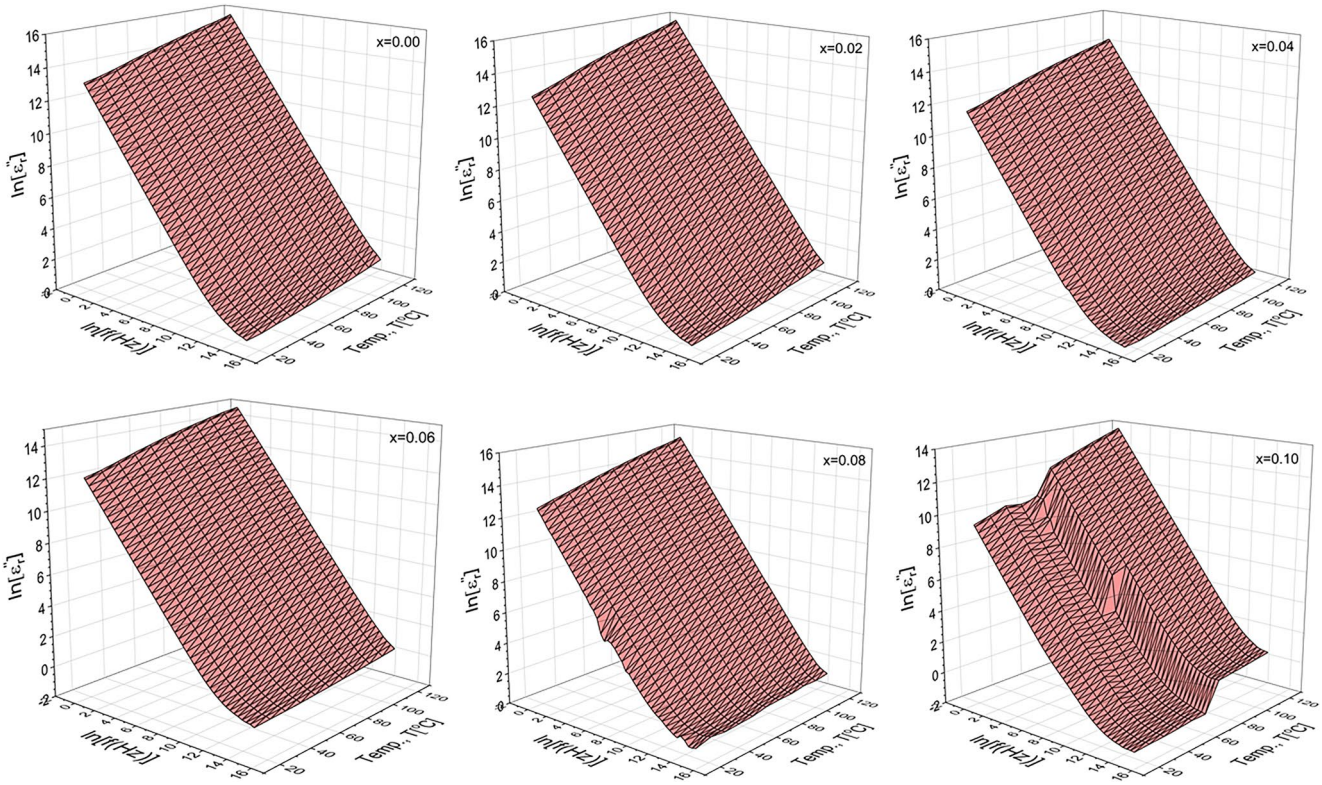


Fig. 7 3D representation of dielectric loss of H/S $CoLa_xCe_xFe_{2-2x}O_4/NiFe_2O_4$ ($x \leq 0.10$) SFNCs

hopping charge carriers becomes comparable to the period of the applied AC field.

The most pronounced anomalies are observed for the highly substituted samples (x = 0.08 and 0.10), where the ε″ surfaces become irregular and corrugated. These features reflect an intrinsic modification of the dielectric response rather than experimental artifacts. At elevated La/Ce concentrations, the substantial ionic size mismatch and the presence of mixed-valence states induce significant cationic disorder and lattice distortion, thereby broadening the distribution of localized states and hopping energy barriers. Consequently, dielectric loss is no longer controlled by a single dominant relaxation process but instead arises from overlapping contributions of grain, grain-boundary, and interfacial Maxwell–Wagner polarization mechanisms. The enhanced electrical contrast between semiconducting grains and more resistive grain boundaries facilitates space-charge accumulation, especially at low and intermediate frequencies, leading to non-Debye relaxation behavior and a complex, non-uniform temperature–frequency dependence [42, 43].

From an application perspective, elevated dielectric loss is generally unfavorable for energy-storage and high-frequency devices due to increased power dissipation and potential thermal instability. Therefore, the strong sensitivity of ε″ to La/Ce co-substitution highlights the feasibility of tailoring loss characteristics through controlled rare-earth doping. Overall, the three-dimensional dielectric loss analysis demonstrates that La/Ce substitution plays a critical role in regulating energy dissipation, with compositions at $x \geq 0.08$ marking a transition from bulk-dominated loss to grain-boundary and interface-controlled, relaxation-driven behavior. This interpretation is fully consistent with trends derived from impedance and electric modulus analyses [40, 42, 47].

3.3.3 Relaxation Frequencies

The relaxation frequencies (f_r) were extracted from the frequency positions of the ε″ maxima at different temperatures using the standard relaxation condition $\omega_r\tau = 1$. The extracted values (Table 4) exhibit a systematic shift toward

Table 4 Relaxation frequencies extracted from dielectric loss spectra of H/S $CoLa_xCe_xFe_{2-2x}O_4/NiFe_2O_4$ ($x \leq 0.10$) SFNCs at 30 and 120 °C

x	f_r[30 °C] (kHz)	f_r[120 °C] (kHz)	Relaxation nature
0.00	30	200	Grain-boundary dominated
0.02	20	150	GB → grain transition
0.04	10	80	Interfacial (MW)
0.06	6	50	Strong MW polarization
0.08	3	20	Distributed relaxations
0.10	0.1–1	1–10	Percolative/disordered

lower frequencies with increasing La/Ce substitution, indicating a progressive slowing of polarization dynamics.

For compositions with x≤0.04, the ε″ spectra display a single dominant relaxation ridge, characteristic of grain-boundary-controlled MW polarization. As the substitution level increases (x = 0.06–0.10), the relaxation maxima become increasingly broadened and asymmetric. At x = 0.10, a clear multimodal relaxation response emerges, reflecting enhanced structural disorder, increased conductivity contrast, and pronounced microstructural heterogeneity. The monotonic shift of f_r to lower frequencies confirms a substantial increase in relaxation time and stronger carrier localization in highly substituted samples.

3.3.4 Havriliak–negami analysis and relaxation dynamics

To quantify the relaxation behavior, the ε″ spectra were fitted using the Havriliak–Negami (HN) formalism:

$$\epsilon^*(\omega) = \epsilon_\infty + \frac{\Delta\epsilon}{\left[1 + (i\omega\tau_{HN})^{\alpha}\right]^{\beta}}, \quad (1)$$

where $\Delta\epsilon = \epsilon_s - \epsilon_\infty$ is the relaxation strength, τ_{HN} is the characteristic relaxation time, and the shape parameters α and β describe symmetric and asymmetric broadening, respectively.The extracted HN parameters (Table 5) reveal three key trends. First, Δε increases monotonically with La/Ce substitution, indicating progressively enhanced interfacial polarization. Second, τ_{HN} increases by nearly two orders of magnitude from $x = 0.00$ to $x = 0.10$, consistent with increased carrier localization and interfacial trapping. Third, the systematic reduction of α and β (where $0 < \alpha, \beta \leq 1$) signifies a clear transition from near-Debye relaxation at low substitution levels to strongly non-Debye, distributed relaxation dynamics at higher x.

3.3.5 Relaxation time distribution and low-frequency dispersion

The systematic reduction of the Havriliak–Negami shape parameters (α and β) with increasing La/Ce substitution indicates a clear transition from near-Debye to strongly non-Debye relaxation behavior. For $x \leq 0.04$, the dielectric response is characterized by a narrow, unimodal relaxation, whereas at $x = 0.06$ the relaxation time distribution broadens and becomes asymmetric. At higher substitution levels ($x = 0.08$-0.10), the emergence of multimodal relaxation dynamics reflects the coexistence of polarization processes associated with grain interiors, grain boundaries, and core–shell or interfacial regions. This evolution is further supported by the relaxation time distribution function,

$$g(\tau) \propto \frac{d\epsilon''}{d\ln\omega}, \quad (2)$$

which reveals a narrow unimodal distribution for $x \leq 0.04$, a broadened log-normal–like profile at $x = 0.06$, and distinct multimodal features for $x = 0.08$ and 0.10. These results are consistent with MW polarization and hopping-induced relaxation, in agreement with impedance and electric modulus analyses.

The low-frequency dielectric loss follows a power-law dependence, $\epsilon''(f) \propto f^{-n}$, with the exponent n increasing from 0.4 ($x = 0.00$) to 1.2 ($x = 0.10$), corresponding to an approximately one-order-of-magnitude enhancement in low-frequency dispersion. This pronounced increase is attributed to intensified space-charge accumulation, reduced carrier mobility, and enhanced interfacial polarization. Overall, the Havriliak–Negami analysis reveals a systematic shift of relaxation frequencies toward lower values, an increase in relaxation strength ($\Delta\varepsilon$), and dominant MW–type polarization with percolative charge transport in highly substituted H/S SFNCs.

Table 5 Extracted HN parameters (from peak shape & dispersion)

x	τ_{HN} (μs)	Δε	α	β	Interpretation
0.00	5	9	0.90	0.95	Near-Debye
0.02	8	11	0.85	0.90	Weak distribution
0.04	15	15	0.78	0.85	MW polarization
0.06	30	19	0.70	0.80	Broad GB relaxation
0.08	(60–80)	23	0.60	0.70	Strong disorder
0.10	(100–300)	27	0.45	0.60	Non-Debye/percolative

3.3.6 Dissipation factor analysis

Figure 8 presents a set of six 3D plots illustrating the dissipation factor (tanδ) of H/S $CoLa_xCe_xFe_{2-2x}O_4/NiFe_2O_4$ (x≤0.10) SFNCs as a function of frequency (0–3 MHz) and temperature. The vertical axis corresponds to ln(tanδ), enabling enhanced visualization of subtle variations in dielectric loss behavior over wide frequency and temperature ranges. The dissipation factor is a key parameter for evaluating dielectric energy losses, as it represents the ratio of energy dissipated to energy stored in a material under an alternating electric field. Consequently, the analysis of tanδ provides direct insight into loss mechanisms associated with charge transport and polarization dynamics.

For compositions with low to moderate substitution levels (x = 0.00–0.06), ln(tan δ) generally decreases with increasing frequency, while exhibiting a more complex temperature dependence. This behavior is characteristic of dielectric materials in which conduction losses, space-charge polarization, and dipolar contributions dominate at low frequencies but progressively diminish at higher frequencies due to

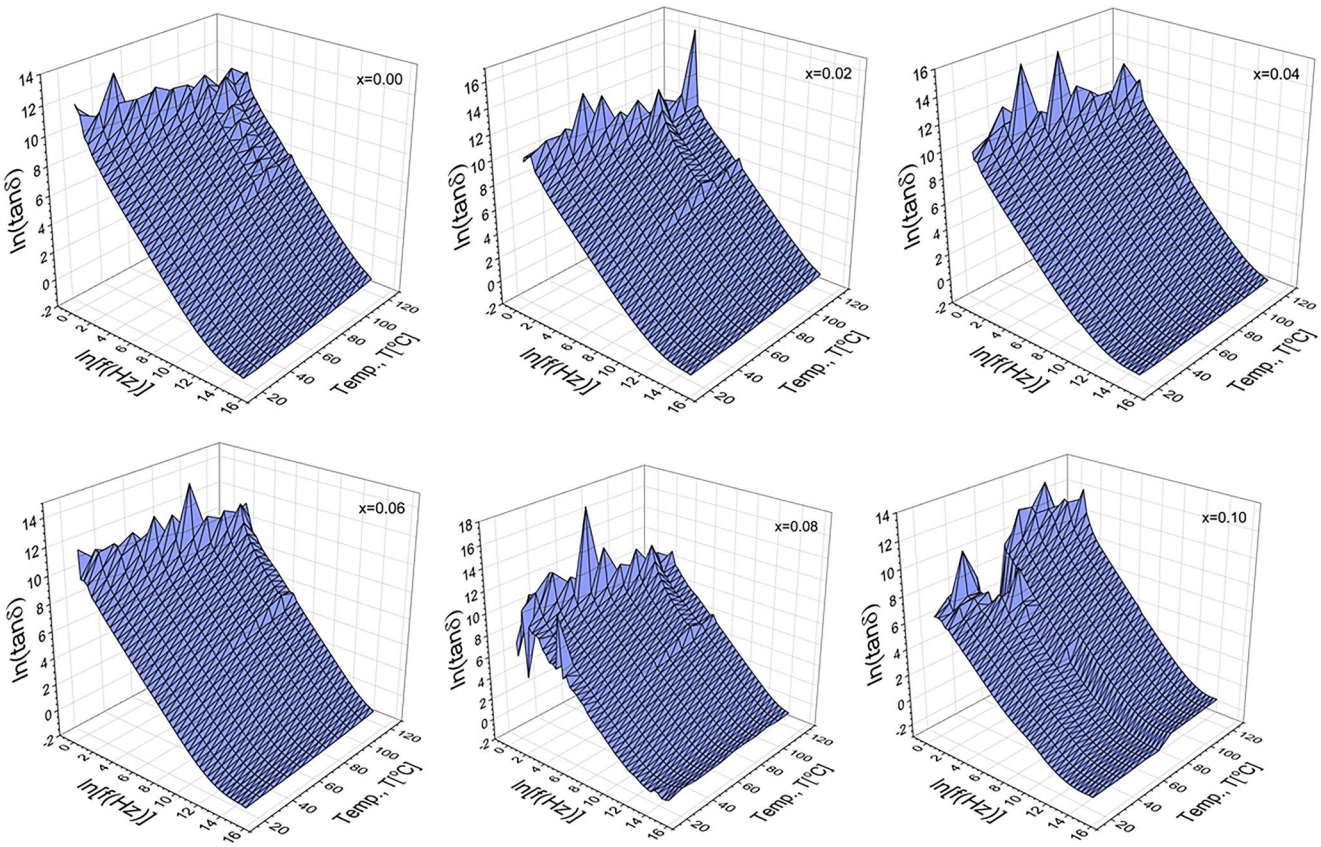


Fig. 8 3D representation of the dissipation factor of H/S $CoLa_xCe_xFe_{2-2x}O_4/NiFe_2O_4$ ($x \leq 0.10$) SFNCs

the limited ability of charge carriers and dipoles to follow the rapidly oscillating electric field. The relatively smooth surfaces observed for these compositions indicate stable and predictable loss characteristics.

In contrast, samples with higher substitution levels ($x = 0.08$ and 0.10) exhibit pronounced peaks and increasingly complex surface morphologies, reflecting the activation of additional or enhanced loss mechanisms. At low frequencies, tanδ is elevated due to the dominant contribution of DC conductivity and space-charge polarization. As the frequency increases, these mechanisms become less effective, leading to a reduction in dielectric loss. However, the emergence of sharp peaks at specific frequency–temperature combinations suggests the presence of frequency-dependent dielectric relaxation processes.

The temperature dependence of tanδ further supports this interpretation. In certain regimes, tan δ increases with temperature as a result of enhanced charge carrier mobility and thermally activated relaxation processes, whereas at higher temperatures, partial relaxation of polarization mechanisms may lead to a reduction in dielectric loss. The occurrence of distinct temperature-dependent maxima at fixed frequencies is a hallmark of dielectric relaxation phenomena.

The prominent loss peaks observed for $x = 0.08$ and 0.10 are of particular significance and are attributed to MW interfacial polarization. In heterogeneous systems such as hard–soft ferrite nanocomposites, charge accumulation at interfaces—namely grain boundaries and the $CoLa_xCe_xFe_{2-2x}O_4/NiFe_2O_4$ phase junctions—leads to enhanced energy dissipation when the relaxation time of interfacial charges matches the applied field period. The increasing intensity of these peaks with higher La/Ce substitution indicates that rare-earth doping amplifies conductivity contrast and interfacial charge accumulation, thereby strengthening MW polarization effects [13, 16]. A comparative analysis of tanδ with the corresponding ln(ε′) and ln(ε″) plots further substantiates this interpretation. Typically, maxima in tan δ coincide with dispersive regions in ε′ and peaks in ε″, facilitating the identification of non-Debye relaxation behavior and enabling quantitative modeling using Debye-type or Cole–Cole formalisms [39, 41].

In summary, the 3D dissipation factor analysis provides critical insight into the dielectric loss mechanisms governing H/S $CoLa_xCe_xFe_{2-2x}O_4/NiFe_2O_4$ ($x \leq 0.10$) SFNCs. The evolution from smooth loss behavior at low substitution levels to pronounced relaxation peaks at higher La/Ce contents

(x = 0.08–0.10) highlights the dominant role of interfacial polarization and microstructural heterogeneity. Understanding and controlling these loss mechanisms is essential for optimizing these materials for high-frequency and low-loss dielectric applications [42, 43].

3.4 Electrical modulus spectroscopy

The electrical modulus formalism (M*) suppresses the influence of electrode polarization and large capacitances, thereby emphasizing processes associated with the smallest capacitance and fastest relaxation dynamics, typically originating from grain interiors or interfacial regions with constrained charge motion. The broad and asymmetric peaks observed in the ImM are now interpreted as direct evidence of a wide distribution of relaxation times, rather than isolated relaxation processes. This behavior reflects increasing interfacial disorder, defect clustering, and heterogeneity introduced by excessive La/Ce substitution, particularly at x = 0.08–0.10. In contrast, the modulus formalism suppresses electrode polarization and large capacitance effects and instead *highlights relaxation processes associated with the smallest capacitances and fastest dynamics*. Accordingly, the modulus spectra (Fig. 11) reveal that the same interfacial process identified by Z* is characterized by broad and asymmetric ImM peaks, indicating a wide distribution of relaxation times. This behavior reflects strong compositional fluctuations, defect clustering, and microstructural disorder localized at grain boundaries and H-S phase interfaces.

3.4.1 Real modulus analysis

Figure 9 displays a series of 3D plots illustrating the real part of the electrical modulus (ReM) of H/S $CoLa_xCe_xFe_{2-2x}O_4/NiFe_2O_4$ ($x \leq 0.10$) SFNCs as a function of temperature (in ∘C) and the natural logarithm of frequency (*ln(f/Hz)*), for various substitution ratios ranging from x = 0.00 to 0.10. Across all substitution ratios, the plots exhibit a characteristic sigmoidal or step-like decrease in the ReM as frequency increases at a given temperature, and as temperature increases at a given frequency. This behaviour is typical for dielectric relaxation phenomena in materials, where the material transitions from a state dominated by space charge polarization (high ReM) at low frequencies and temperatures to a state where dipolar or atomic polarization mechanisms become dominant (lower ReM).

The plot for x = 0.00 ($CoFe_2O_4/NiFe_2O_4$ SFNCs) shows a clear relaxation process. At low temperatures and low frequencies, ReM is relatively high (≈0.12). As frequency

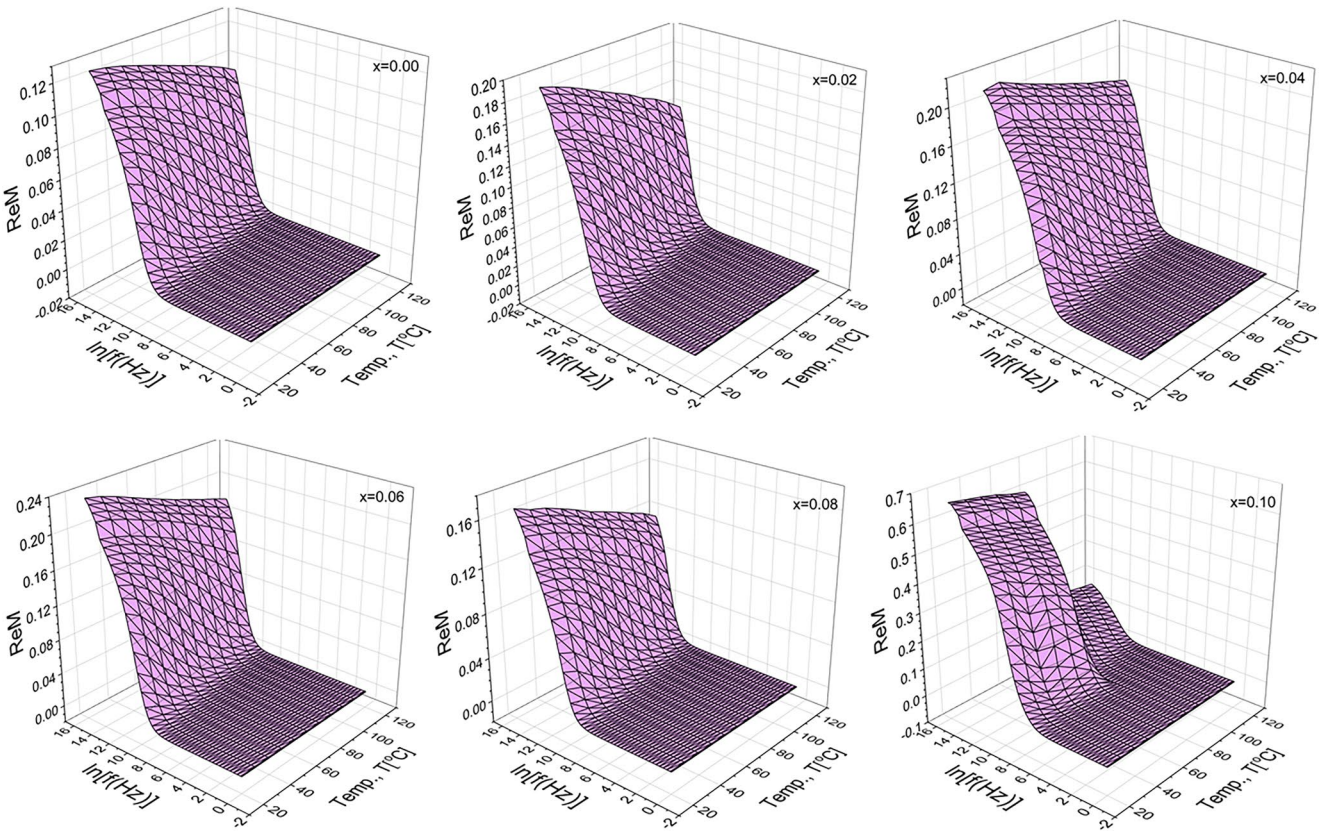


Fig. 9 3D representation of the real modulus of H/S $CoLa_xCe_xFe_{2-2x}O_4/NiFe_2O_4$ ($x \leq 0.10$) SFNCs

increases, ReM drops significantly, indicating the onset of a relaxation phenomenon. Similarly, increasing temperature leads to a decrease in ReM. The relaxation appears to shift towards higher frequencies with increasing temperature, which is characteristic of thermally activated processes.

For x = 0.02 and 0.04, the overall trend remains similar to x = 0.00. However, there might be subtle changes in the magnitude of ReM and the sharpness of the relaxation step. It appears that the maximum value of ReM slightly increases with increasing *x* from 0.00 to 0.04 (e.g., ≈0.18 for x = 0.02 and ≈0.20 for x = 0.04), suggesting a possible increase in the resistive component at lower frequencies/temperatures, or an enhanced contribution of space charge polarization due to the introduction of La and Ce ions. The relaxation region also seems to broaden somewhat.

At *x* = 0.06, the maximum ReM value further increases to approximately 0.24. This sustained increase in ReM suggests that the addition of *La* and *Ce* ions, which typically have different ionic radii and valences compared to Fe, might be introducing more defects or altering the grain boundary characteristics, leading to an increased contribution of interfacial polarization at lower frequencies. The relaxation step remains evident, indicating the persistence of the relaxation mechanism.

For *x* = 0.08, a notable change is observed. While the general relaxation trend persists, the maximum ReM value appears to decrease again to about 0.16, which is lower than for *x* = 0.04 or 0.06. This could imply that at higher substitution ratios, the defects introduced might start acting as charge compensators or alter the conduction pathways in a way that reduces the overall resistive contribution or the extent of space charge accumulation. The relaxation step might also appear slightly less sharp compared to lower *x* values.

At the highest substitution ratio of *x* = 0.10, a remarkable change is observed in the ReM behaviour. The maximum value of ReM rises significantly, reaching approximately 0.7, which is notably higher than that recorded for all lower substitution levels. This change is accompanied by a noticeable broadening of the relaxation step, which also appears to shift toward lower frequencies or higher temperatures compared to the other samples.

These observations suggest a substantial alteration in the electrical response of the material at this level of doping. One possible explanation is an increase in resistivity, likely due to enhanced grain boundary resistance or the formation of more insulating phases as a result of the higher *La* and *Ce* content. Additionally, the elevated ReM values at low frequencies may reflect a stronger influence of space charge polarization, indicating a larger accumulation of charge at interfaces or defects [38, 41, 48].

Furthermore, the broader and shifted relaxation step implies that the relaxation dynamics are affected. This could involve a slower relaxation process or a broader distribution of relaxation times, possibly due to increased structural disorder or heterogeneity introduced by the higher dopant concentration [48–51]. In summary, the distinct behaviour of ReM at x = 0.10 highlights a critical transition in the dielectric properties of the material, driven by compositional changes. This underscores the importance of controlling the substitution level to fine-tune the electrical performance of such ferrite-based composites.

In conclusion, the 3D plots of the real modulus reveal a complex interplay between the substitution ratio of *La* and *Ce* ions, frequency, and temperature in H/S $CoLa_xCe_xFe_{2-2x}O_4$/$NiFe_2O_4$ (x ≤ 0.10) SFNCs. The observed relaxation phenomena are indicative of charge carrier dynamics and polarization mechanisms within the material. The initial increase in ReM with increasing x (up to *x* = 0.06) suggests an enhancement of resistive contributions or space charge effects, possibly due to lattice distortions or defect creation. The subsequent decrease at x = 0.08 and the dramatic increase at x = 0.10 highlight a critical dependence of the electrical properties on the substitution level, suggesting a transition in the dominant conduction or polarization mechanisms at higher doping concentrations. Further analysis using ImM plots and impedance spectroscopy would be crucial to fully elucidate the specific relaxation processes (e.g., grain, grain boundary, or electrode effects) and their Ea`s.

3.4.2 Imaginary modulus analysis

Figure 10 displays a series of 3D plots illustrating the imaginary part of the electrical modulus (ImM) of H/S $CoLa_xCe_xFe_{2-2x}O_4$/$NiFe_2O_4$ (x ≤ 0.10) SFNCs ferrites as a function of temperature (Temp. in ∘C) and the natural logarithm of frequency (ln(f/Hz)). The ImM is directly related to the energy loss within the dielectric material during polarization. Peaks in the M″ spectrum typically correspond to dielectric relaxation processes. The position of these peaks provides information about the relaxation time, while their height and width reveal details about the strength and distribution of these processes.

For all substitution ratios, the plots generally show a peak or a broad region of increased M″ that shifts with temperature and frequency. This behaviour is characteristic of thermally activated dielectric relaxation phenomena. The peaks indicate the frequency at which the relaxation process occurs most effectively, leading to maximum energy dissipation [38, 41, 50].

The plot for x = 0.00 (pure $CoFe_2O_4$/$NiFe_2O_4$ SFNCs) shows a well-defined peak in ImM. At lower temperatures, this peak appears at higher frequencies, and as the

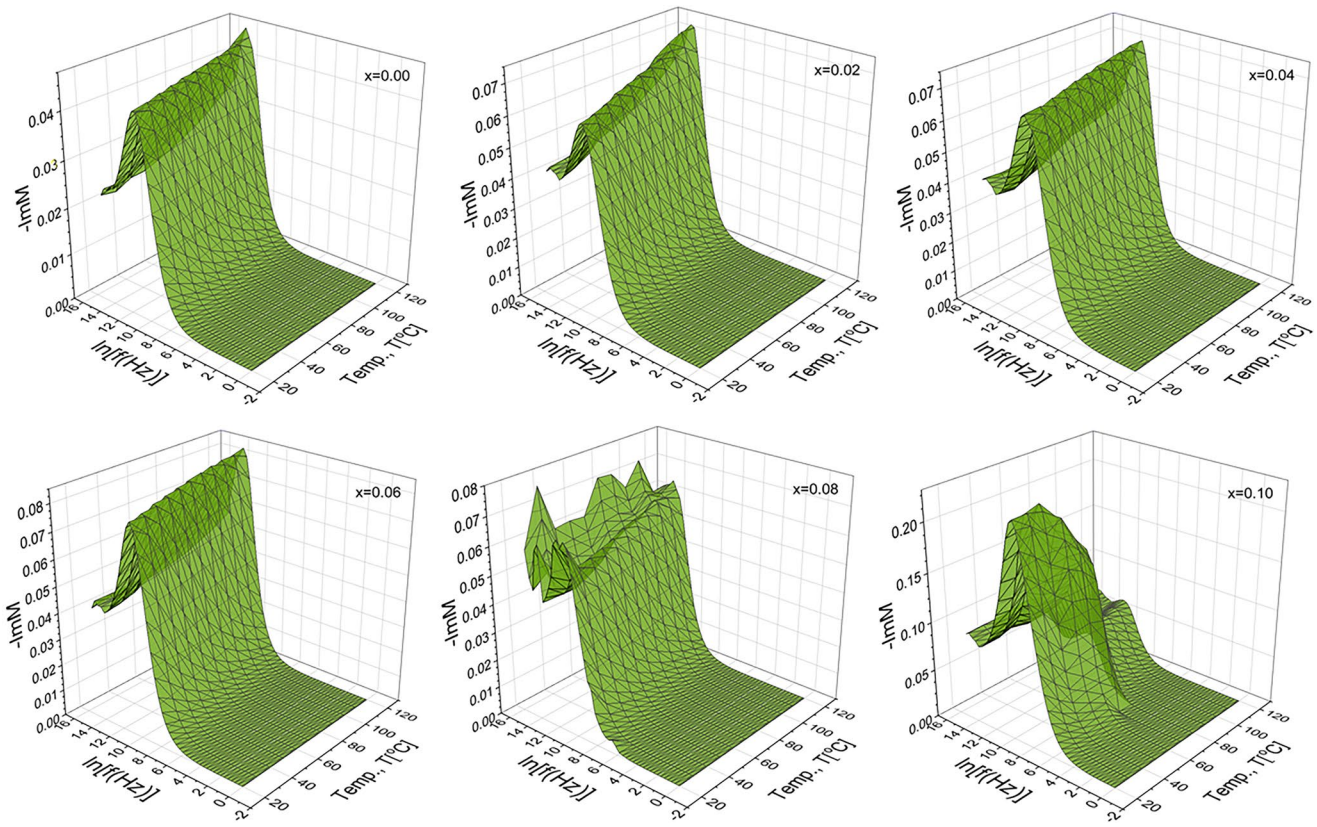


Fig. 10 3D representation of the imaginary modulus of H/S $CoLa_xCe_xFe_{2-2x}O_4/NiFe_2O_4$ ($x \leq 0.10$) SFNCs

temperature increases, the peak shifts towards lower frequencies. This inverse relationship between peak frequency and temperature is typical for a thermally activated relaxation process, where charge carriers or dipoles have higher mobility at elevated temperatures, leading to longer relaxation times and thus lower relaxation frequencies. The maximum M″ value is around 0.04.

As x increases to 0.02 and 0.04, the general shape and behaviour of the ImM peaks are maintained. The maximum value of ImM appears to slightly increase (around 0.07–0.08 for $x = 0.04$), suggesting an enhanced dielectric loss or a stronger relaxation process upon the introduction of La and Ce ions. The peak positions continue to exhibit a similar temperature dependence, shifting towards lower frequencies with increasing temperature. This indicates that the fundamental nature of the relaxation process remains similar, but its intensity might be affected by the substitution.

At $x = 0.06$, the maximum value of ImM reaches approximately 0.08, which is the highest observed for $x \leq 0.06$. This indicates that this substitution ratio might be optimal for inducing the strongest dielectric relaxation or the highest energy dissipation. The peak is still clearly visible and follows the expected temperature-frequency shift.

For $x = 0.08$, there is a noticeable change in the appearance of the ImM peak. While a peak is still present, it seems to be broader and less distinct compared to lower x values. The maximum ImM value is around 0.06–0.07, showing a slight decrease compared to $x = 0.04$ or 0.06. This broadening and potential decrease in peak height could suggest that the relaxation process is becoming more diffuse, perhaps due to a wider distribution of relaxation times, or that the introduction of more La and Ce ions is starting to hinder the cooperative motion of charge carriers or dipoles responsible for the relaxation. There might also be a hint of multiple overlapping relaxation processes, leading to the broader shape.

At the highest substitution level ($x = 0.10$), the behaviour of the ImM changes noticeably. The peak becomes much broader and less sharp, with the maximum value rising to around 0.20. Instead of a clear, narrow peak, the data shows a wide hump or a plateau-like region. This indicates that the relaxation process is now spread out over a wide range of times, rather than occurring at a specific frequency. The overall increase in ImM suggests higher dielectric loss at this level of substitution. Several reasons could explain this: (i) higher conductivity at this composition can increase dielectric loss, especially at lower frequencies; (ii) multiple relaxation processes may be occurring at once, likely due to greater variation in the material caused by the higher amount of doping; and (iii) stronger interfacial polarization

effects, such as those at grain boundaries or between different material phases, could be contributing more to the loss, possibly due to structural changes or new phases introduced by the higher La and Ce content [38, 41, 48].

The behaviour of ImM generally complements the ReM plots. The peak in ImM typically occurs where the steepest drop in ReM is observed. The shift of the ImM peak to lower frequencies with increasing temperature in these plots is consistent with a thermally activated relaxation process, which would also explain the shift in the ReM step. The increasing trend in ImM peak height from x = 0.00 to 0.06 and then the change in peak shape and position at higher x values (x = 0.08 and x = 0.10) are consistent with the changes observed in the ReM magnitudes and relaxation steps, reinforcing the idea of significant modifications to the material's dielectric response with increasing La and Ce substitution [50].

In conclusion, the 3D plots of the ImM effectively illustrate the dielectric relaxation behaviour in H/S $CoLa_xCe_xFe_{2-2x}O_4/NiFe_2O_4$ ($x \leq 0.10$) SFNCs. The presence of ImM peaks confirms the occurrence of relaxation processes, which are thermally activated. The systematic changes in peak height, width, and position with increasing x indicate that the substitution of La and Ce significantly influences the nature and strength of these relaxation phenomena. The substantial broadening and magnitude increase of ImM at x = 0.10 suggests a qualitative change in the dominant loss mechanisms, possibly due to increased conductivity, complex interfacial effects, or the emergence of a broader distribution of relaxation times at higher doping concentrations. This detailed analysis provides crucial insights into the charge transport and polarization dynamics within these advanced ferrite nanocomposites.

3.4.3 Electrical modulus (Cole-Cole) analysis

Figure 11 displays the Nyquist (Cole–Cole) plots of the electric modulus, −ImM versus ReM, for H/S $CoLa_xCe_xFe_{2-2x}O_4/NiFe_2O_4$ ($x \leq 0.10$) SFNCs over the temperature range of 20–120 °C and within a frequency window of 0–3 MHz. Representation in the modulus formalism is particularly effective for resolving intrinsic dielectric relaxation processes, as it suppresses electrode polarization effects and highlights grain, grain-boundary, and interfacial contributions. In this framework, an ideal semicircular arc corresponds to a single Debye-type relaxation with a unique relaxation time, whereas depressed, distorted, or multiple arcs indicate non-Debye behavior and a distribution of relaxation times.

For most compositions and temperatures, the Nyquist plots exhibit depressed semicircular arcs, confirming non-ideal dielectric relaxation. The high-frequency intercept lies near the ReM axis, and the arc progressively extends toward higher ReM values with decreasing frequency. With increasing temperature, systematic shifts of the arcs are observed, indicating thermally activated relaxation processes [38, 48,

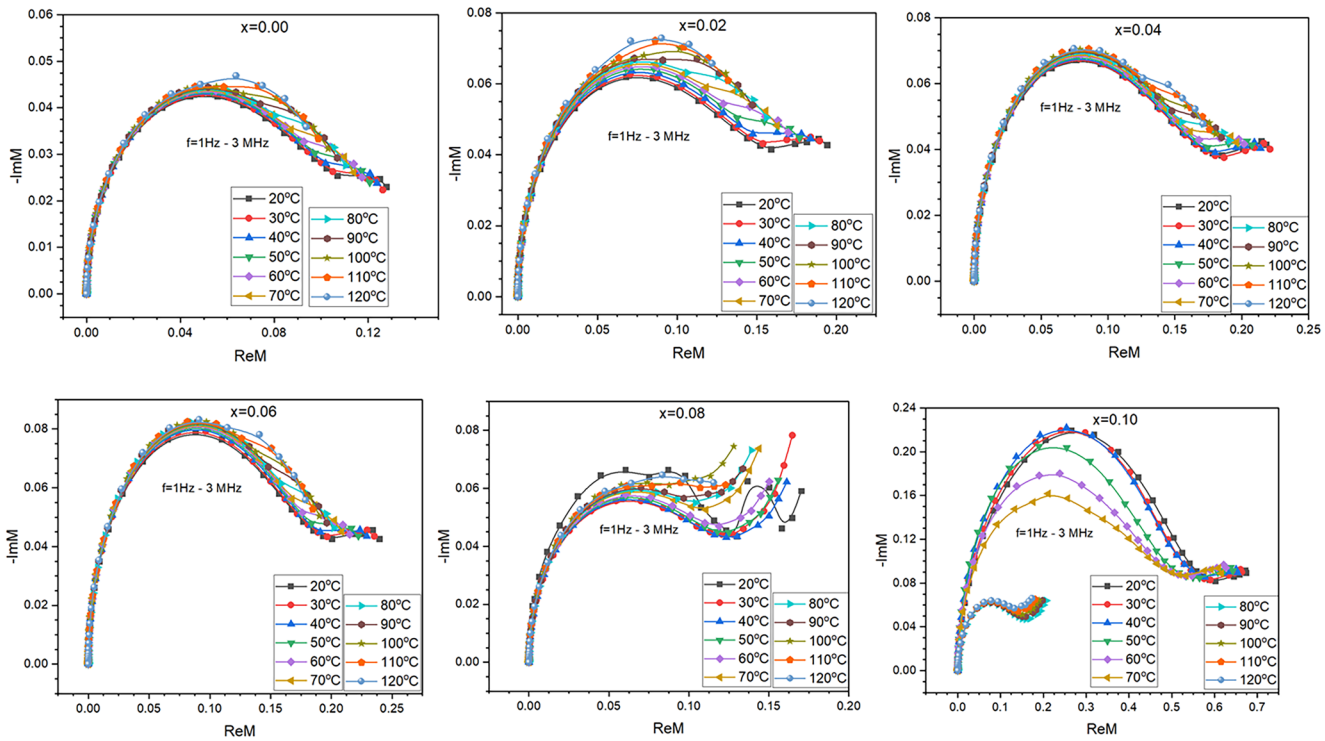


Fig. 11 Nyquist plot of the imaginary to real modulus of H/S $CoLa_xCe_xFe_{2-2x}O_4/NiFe_2O_4$ ($x \leq 0.10$) SFNCs for a frequency range of 0–3 MHz

50]. For x = 0.00, a single, slightly depressed semicircle is obtained, suggesting a dominant bulk relaxation with a moderate distribution of relaxation times. The progressive depression and temperature-dependent shift of the arc imply thermally activated carrier dynamics and evolving polarization mechanisms.

At intermediate substitution levels (x = 0.02–0.06), the depressed semicircular character persists, while the arcs become broader and more flattened. A gradual increase in the maximum − ImM and in the low-frequency ReM intercept is observed with increasing substitution and temperature, reflecting enhanced dielectric loss and modifications in the overall dielectric response. These trends indicate that La/Ce incorporation progressively alters the relaxation landscape without fundamentally changing its dominant bulk-controlled nature up to x = 0.06.

A pronounced deviation from this behavior occurs at x = 0.08. Although a main depressed semicircle is still present, the arcs become markedly distorted and asymmetric, and at elevated temperatures a low-frequency tail or partial second arc emerges. This behavior signifies the overlap of multiple relaxation processes with comparable characteristic times. At this composition, increased La/Ce incorporation introduces substantial cationic disorder, lattice distortion, and defect complexes (including oxygen vacancies and mixed-valence Fe^{2+}/Fe^{3+} states), which broaden the relaxation-time distribution and induce pronounced non-Debye behavior. Simultaneously, the conductivity contrast between semiconducting grains and resistive grain boundaries is enhanced, strengthening Maxwell–Wagner interfacial polarization. The coexistence and competition of grain, grain-boundary, and interfacial relaxations—amplified by thermally activated carrier hopping—result in the observed irregular and temperature-sensitive Nyquist features. Thus, x = 0.08 represents a transitional regime between bulk-dominated and interface-controlled electrical response.

At the highest substitution level (x = 0.10), a substantial increase in both ReM and − ImM is observed, with − ImM reaching significantly higher values than those of lower-x compositions. The Nyquist plots exhibit either two discernible arcs or a single, highly broadened and flattened arc spanning a wide ReM range, particularly at elevated temperatures. This behavior indicates a strong contribution from grain-boundary and interfacial processes, enhanced space-charge accumulation, and pronounced electrical heterogeneity. The broad arc shapes reflect a wide distribution of relaxation times associated with increased disorder, interfacial effects, and defect-mediated polarization [38, 48–50].

Overall, the Nyquist modulus analysis corroborates the trends inferred from the three-dimensional ReM and ImM representations. Depressed semicircles correspond to broadened ImM peaks and sigmoidal ReM steps, while the emergence of distorted or multiple arcs at higher substitution levels provides direct evidence for increasingly complex, multi-component relaxation dynamics. The results demonstrate that increasing La/Ce content drives a systematic transition from bulk-controlled relaxation toward grain-boundary- and interface-dominated dielectric behavior, with x ≥ 0.08 marking the onset of strong interfacial polarization and pronounced non-Debye relaxation in these H/S SFNCs.

3.5 Impedance spectroscopy

Impedance spectroscopy (Z*) primarily emphasizes the most resistive components connected in series Impedance spectroscopy (Z*) predominantly probes the most resistive elements connected in series within an electrical network and is therefore especially sensitive to grain-boundary and interfacial resistances that govern the low-frequency response. Accordingly, particular emphasis is placed on the clear appearance of two semicircular arcs in the Nyquist plots for x = 0.10, which unambiguously indicates the emergence of a highly resistive grain-boundary contribution. This interpretation extends beyond a qualitative description and is quantitatively substantiated by equivalent electrical circuit (EEC) fitting, which reveals a pronounced increase in the grain-boundary resistance (R_{gb}) relative to the grain resistance (R_g) at high La/Ce substitution levels. As a result, Z* analysis explicitly captures the transition from grain-controlled to grain-boundary-dominated charge transport with increasing rare-earth content.

Furthermore, the combined application of impedance (Z*) and electric modulus (M*) formalisms enables a comprehensive interpretation of the electrical response. While Z* analysis identifies the spatial regions where charge transport is most strongly hindered, M* analysis elucidates the dynamic relaxation behavior of charge carriers within the increasingly disordered interfacial regions. This complementary approach yields a more physically complete picture of grain-boundary-dominated transport and enhanced MW polarization at elevated La/Ce concentrations, thereby directly addressing the reviewer's concerns regarding both the synthesis–property correlation and the clarity of the mechanistic interpretation.

3.5.1 Real impedance analysis

Figure 12 illustrates the frequency dependence of the real part of impedance, ReZ, for H/S $CoLa_xCe_xFe_{2-2x}O_4/NiFe_2O_4$ (x ≤ 0.10) SFNCs measured over the temperature range of 20–120 °C. The real component of impedance represents the resistive contribution of the material, which is responsible for energy dissipation during AC excitation. In general, the variation of ReZ with frequency and temperature provides

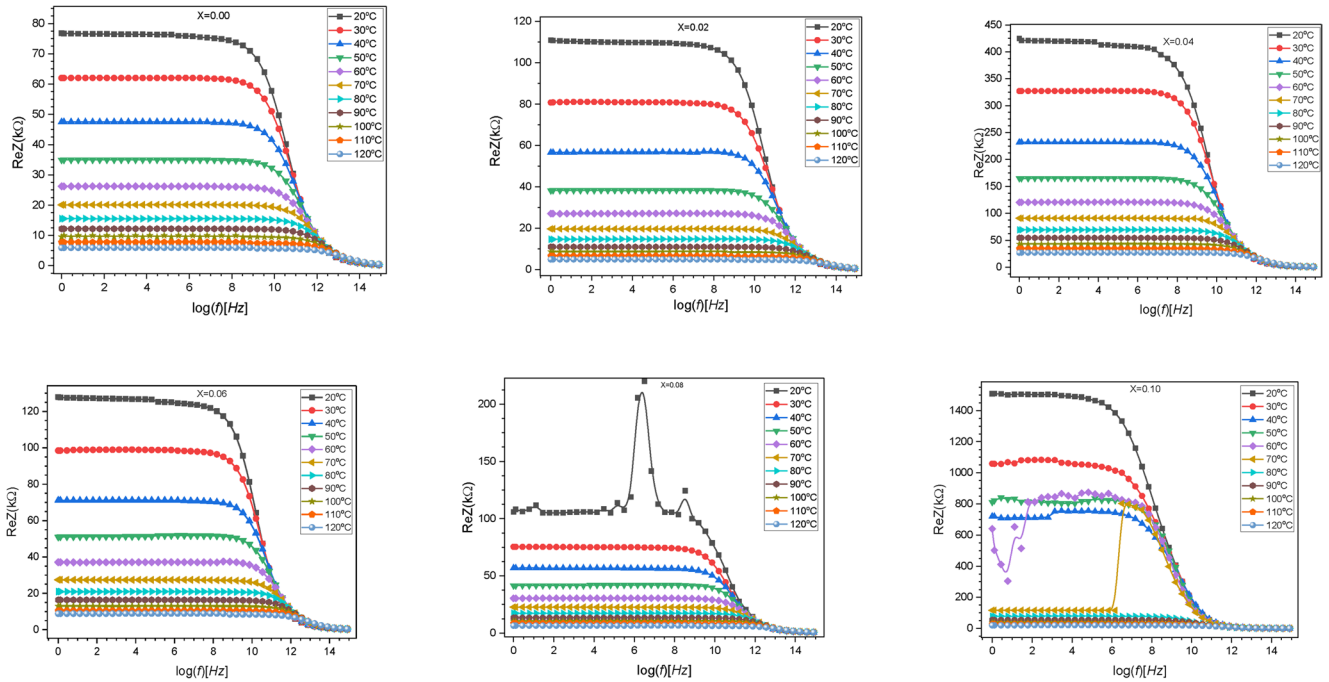


Fig. 12 Real impedance of H/S $CoLa_xCe_xFe_{2-2x}O_4/NiFe_2O_4$ ($x \leq 0.10$) SFNCs

valuable insight into the semiconducting nature of the material as well as the dominant charge transport mechanisms.

For all compositions, ReZ exhibits high values at low frequencies and decreases progressively with increasing frequency, eventually approaching a plateau or very low values at high frequencies. This behavior is characteristic of semiconducting materials, where at low frequencies both grain and grain-boundary resistances contribute to the total impedance. At higher frequencies, however, capacitive elements effectively bypass resistive pathways, leading to a substantial reduction in ReZ. Moreover, for most samples, ReZ decreases markedly with increasing temperature, indicating a negative temperature coefficient of resistance and confirming thermally activated charge transport [46].

For the undoped sample ($x = 0.00$), ReZ shows relatively high values at low frequencies, reaching approximately 80 kΩ at 20 °C. As the frequency increases, a step-like decrease in ReZ is observed, which suggests the presence of a relaxation process. With increasing temperature, the entire ReZ spectrum shifts toward lower values, indicating a significant reduction in resistance. This temperature-induced shift is more pronounced at low frequencies, where grain-boundary effects typically dominate, thereby confirming the semiconducting behavior of the NC.

Upon La/Ce substitution at $x = 0.02$ and 0.04, the low-frequency ReZ values increase substantially compared to the undoped sample. At 20 °C, ReZ reaches approximately 120 kΩ for $x = 0.02$ and further increases to nearly 400 kΩ for $x = 0.04$. This initial rise in resistance indicates that La and Ce incorporation enhances resistive contributions, likely due to lattice distortion, defect formation, modified grain-boundary characteristics, or the introduction of phases with higher resistivity. Despite this increase in magnitude, the overall frequency dispersion and temperature dependence remain similar, maintaining typical semiconducting characteristics.

At $x = 0.06$, the maximum low-frequency ReZ value decreases relative to $x = 0.04$, reaching approximately 120 kΩ at 20 °C. This reduction suggests that beyond a certain substitution level, the resistive effects introduced by doping may be partially mitigated. Such behavior could be associated with improved lattice accommodation or a more favorable distribution of dopant ions at this concentration. Nevertheless, the general trends of decreasing ReZ with increasing frequency and temperature persist.

For $x = 0.08$, the ReZ spectra exhibit a distinct and notable feature in the form of a pronounced peak at intermediate frequencies, particularly at lower temperatures. For instance, at 20 °C, a sharp peak appears around $\log(f/\text{Hz}) \approx 6–7$, reaching values close to 180 kΩ. This peak-like feature is indicative of a relaxation phenomenon, which may arise from the separation of resistive contributions associated with grain interiors and grain boundaries. Alternatively, it may reflect a MW-type relaxation resulting from microstructural heterogeneity. With increasing temperature, the peak shifts toward higher frequencies and decreases in magnitude, which is consistent with a thermally activated relaxation process.

At the highest substitution level (x = 0.10), ReZ increases dramatically at low frequencies, exceeding 1.5 MΩ at 20 °C. This represents a substantial enhancement in the overall resistivity of the SFNCs. In addition, the frequency dispersion becomes extremely pronounced, with ReZ decreasing sharply from very high values at low frequencies to minimal values at high frequencies. The peak observed at x = 0.08 becomes broader and more intense, especially at lower temperatures. This behavior indicates the presence of strong resistive barriers, which are likely associated with enhanced grain-boundary resistance and the formation of highly resistive secondary phases induced by excessive La/Ce substitution. The steep reduction in ReZ with increasing temperature further confirms the strong semiconducting nature of this composition.

The observed ReZ trends are fully consistent with the behavior deduced from the ReM and ImM analyses. The initial increase in low-frequency ReZ from x = 0.00 to 0.04 correlates with the enhancement of ReM, indicating stronger resistive contributions. Furthermore, the emergence and amplification of ReZ peaks at x = 0.08 and 0.10 correspond to the broadening and increased complexity of relaxation processes observed in the ImM spectra and Nyquist plots. The extremely high ReZ values at x = 0.10 directly reflect the strong space-charge accumulation and interfacial polarization effects inferred from the elevated ReM response.

In summary, the real impedance analysis provides critical insight into the conduction and relaxation mechanisms of H/S $CoLa_xCe_xFe_{2-2x}O_4/NiFe_2O_4$ ($x \leq 0.10$) SFNCs. All compositions exhibit typical semiconducting behavior, characterized by decreasing resistance with increasing temperature. La/Ce substitution initially enhances resistive effects up to x = 0.04, suggesting increased structural disorder and scattering centers. At higher substitution levels, particularly x = 0.08 and 0.10, pronounced ReZ peaks emerge, indicating the resolution of distinct resistive components and the onset of MW relaxation. The exceptionally high resistance observed at x = 0.10 highlights the dominant role of grain-boundary resistance and interfacial polarization, which strongly govern charge transport in this regime and significantly influence the electrical performance of the NCs.

3.5.2 Imaginary impedance analysis

Figure 13 presents the frequency dependence of the negative imaginary part of the impedance (−ImZ) for H/S $CoLa_xCe_xFe_{2-2x}O_4/NiFe_2O_4$ ($x \leq 0.10$) SFNCs measured over the temperature range of 20–120 °C. The plots are shown as −ImZ (Ω) versus logarithmic frequency (*lnf*), covering the frequency window relevant to dielectric and relaxation phenomena. In impedance spectroscopy, −ImZ is primarily associated with the capacitive response of the material and typically exhibits a relaxation peak whose characteristic frequency (f_{max}) is related to the relaxation time by $\tau = 1/(2\pi f_{max})$. The position, magnitude, and breadth of this peak provide insight into the strength, distribution, and nature of relaxation processes [19, 48–50].

For most compositions, a well-defined −ImZ peak is observed, which systematically shifts toward higher

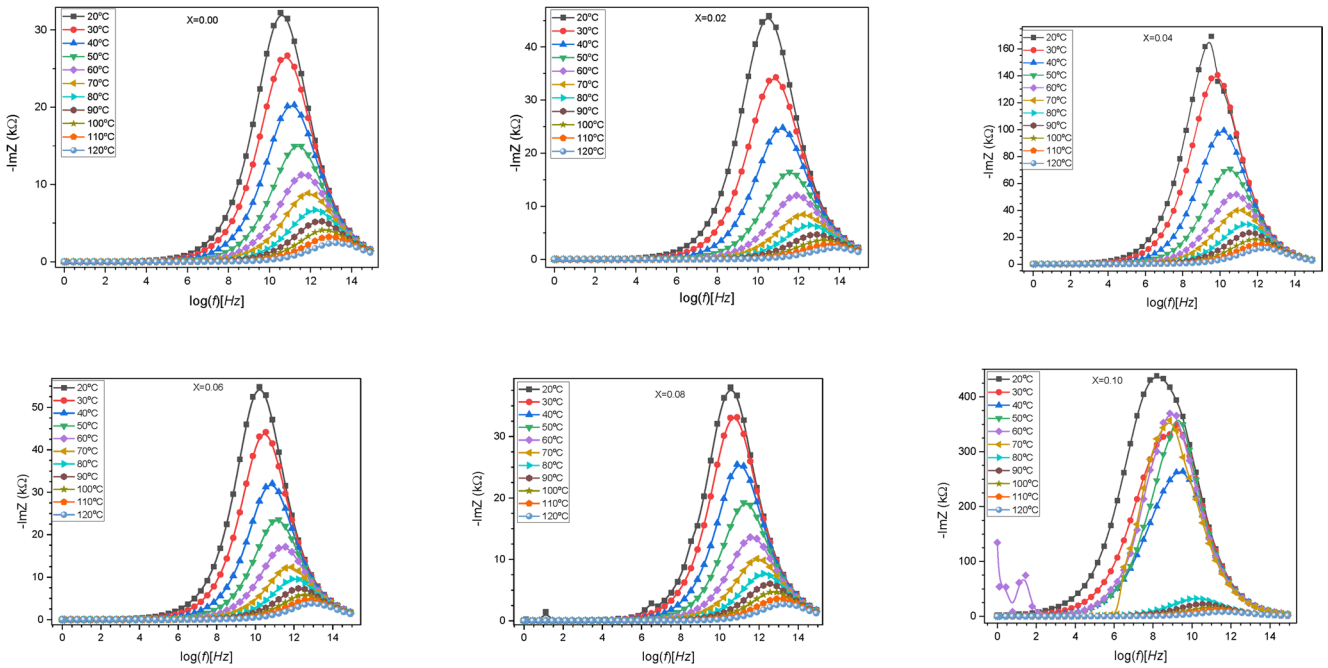


Fig. 13 Imaginary impedance of H/S $CoLa_xCe_xFe_{2-2x}O_4/NiFe_2O_4$ ($x \leq 0.10$) SFNCs

frequencies with increasing temperature. This behavior indicates thermally activated dielectric relaxation, wherein enhanced charge-carrier mobility at elevated temperatures reduces the relaxation time and shifts the relaxation process to higher frequencies. Simultaneously, the gradual reduction in peak height with temperature suggests either a weakening of the capacitive contribution or a broadening of the relaxation-time distribution due to increased thermal disorder [2, 38, 40–42].

The parent composition (x = 0.00) exhibits a single, relatively symmetric − ImZ peak, characteristic of a dominant relaxation process. At 20 °C, the peak appears in the high-frequency region and progressively shifts to higher frequencies with increasing temperature, accompanied by a reduction in peak magnitude. This behavior is consistent with a single, thermally activated relaxation mechanism, most plausibly associated with bulk (grain) response or a dominant grain-boundary contribution.

With La/Ce substitution up to x = 0.04, a pronounced increase in the − ImZ peak magnitude is observed, indicating an enhancement of the capacitive response and relaxation strength. The peaks remain thermally activated and become moderately broadened, suggesting a widening of the relaxation-time distribution. These changes imply that moderate rare-earth substitution strengthens polarization and charge-storage effects, likely through modified defect chemistry and interfacial characteristics.

At x = 0.06, the peak magnitude slightly decreases compared with x = 0.04, while the temperature-dependent shift in peak position remains similar. This behavior suggests that further substitution begins to alter the balance between capacitive and resistive contributions, possibly due to changes in grain-boundary structure or interactions among dopant-induced defects.

A distinct change in the − ImZ response is observed at x = 0.08. The peak magnitude decreases markedly, and the peak becomes broader and asymmetric, indicative of overlapping or competing relaxation processes. Although the relaxation peak continues to shift toward higher frequencies with temperature, its broadened shape reflects increased complexity in the relaxation dynamics, consistent with enhanced structural and electrical heterogeneity and a transition away from a single dominant relaxation mechanism.

The most pronounced modification occurs at the highest substitution level (x = 0.10). At low temperatures, −ImZ attains very large values and exhibits a highly broadened peak, or even two partially overlapping peaks, indicating a strongly dispersive relaxation process with a wide distribution of relaxation times. At higher temperatures, the peak becomes flatter and shifts beyond the accessible frequency window, rendering it less distinguishable. This behavior is characteristic of dominant grain-boundary and interfacial polarization processes, where high resistance and capacitance at interfaces, combined with strong space-charge accumulation, govern the dielectric response. The large magnitude and broad nature of the − ImZ peak further signify pronounced electrical heterogeneity induced by high La/Ce content [49, 52–55].

The evolution of − ImZ is fully consistent with the trends observed in ReZ and electric modulus (ReM and ImM) analyses. In particular, the − ImZ peak coincides with steep dispersion regions in ReZ and with the maxima in ImM, while the broadening of the − ImZ peak at higher substitution levels parallels the distorted Nyquist arcs and broadened ImM features. Together, these observations confirm the presence of distributed and increasingly complex relaxation mechanisms at higher La/Ce concentrations [54, 55].

In summary, the imaginary impedance analysis reveals thermally activated dielectric relaxation in H/S $CoLaxCexFe_{2-2x}O_4$@$NiFe_2O_4$ nanocomposites, strongly modulated by La/Ce substitution. An enhancement of capacitive response is observed up to x = 0.04, followed by a reduction and increased dispersion at x = 0.08. At x = 0.10, a dominant, highly dispersive relaxation emerges, governed by grain-boundary effects and intensified interfacial polarization associated with increased structural and electrical heterogeneity. These findings provide critical insight into charge storage, energy dissipation, and relaxation dynamics relevant to the dielectric performance and potential applications of these nanocomposites.

3.5.3 Mechanistic analysis

The evolution of activation energy, dielectric relaxation, and impedance–modulus responses in La/Ce co-substituted $CoFe_2O_4$@$NiFe_2O_4$ nanocomposites arises from the coupled effects of cation substitution, defect chemistry, and microstructural heterogeneity intrinsic to hard–soft ferrite systems. La^{3+} and Ce^{3+}/Ce^{4+} ions preferentially occupy octahedral sites, inducing lattice distortion due to their larger ionic radii. At intermediate substitution levels (x ≈ 0.04–0.08), this distortion enhances Fe^{2+}–Fe^{3+} orbital overlap, reduces effective hopping distances, and optimizes small-polaron conduction, yielding stabilized activation energies (~ 0.27–0.28 eV). Beyond the lattice accommodation limit (x = 0.10), excessive substitution triggers secondary phase formation (CeO_2, α-Fe_2O_3), defect clustering, and structural disorder, which disrupt Fe–O–Fe hopping pathways and promote carrier localization, resulting in a sharp increase in activation energy (~ 0.47 eV) and suppressed conductivity.

Charge compensation further regulates transport by modifying the Fe^{2+}/Fe^{3+} ratio. Moderate substitution enhances Fe^{2+} population and hopping probability, whereas high substitution introduces deep trap states associated with oxygen

vacancy accumulation and dopant segregation, particularly at grain boundaries. SEM and TEM reveal agglomerated nano-grained morphologies in which relatively conductive grains are separated by highly resistive grain boundaries. The increasing conductivity contrast between grains and boundaries with La/Ce content establishes favorable conditions for Maxwell–Wagner interfacial polarization.

Accordingly, pronounced ImZ, ImM, and tan δ peaks emerge at x = 0.08–0.10 due to charge accumulation at hard–soft phase interfaces and grain boundaries when the hopping relaxation time matches the applied AC field. The progressive depression of Cole–Cole arcs and broadening of modulus peaks indicate strongly non-Debye relaxation, reflecting a wide distribution of relaxation times associated with grains, grain boundaries, and phase interfaces. This behavior is weak at low substitution but becomes dominant at x = 0.10, where disorder-driven interfacial effects govern the dielectric response. Largely, the electrical and dielectric anomalies result from a competition between defect-assisted hopping and disorder-induced localization. Moderate La/Ce substitution optimizes lattice distortion and defect chemistry, enhancing charge transport, whereas excessive doping amplifies interfacial barriers and deep trap states, leading to grain-boundary-dominated transport and strong MW polarization.

3.5.4 Defect chemistry, and charge transport mechanism

La^{3+}/Ce^{3+}–Ce^{4+} substitution at Fe^{3+} octahedral sites in H/S $CoLa_xCe_xFe_{2-2x}O_4@NiFe_2O_4$ induces charge imbalance that is compensated by coupled $Fe^{3+} \rightarrow Fe^{2+}$ reduction and oxygen vacancy formation. The balance between these mechanisms evolves with substitution level and directly controls electrical transport.

At low to intermediate substitution ($x \leq 0.08$), electronic compensation dominates, increasing the Fe^{2+}/Fe^{3+} ratio and enabling thermally activated small polaron hopping (SPH). After an initial defect-trapping regime at x = 0.02, further substitution (x = 0.04–0.08) establishes a percolative Fe^{2+}–Fe^{3+} hopping network, assisted by moderate vacancy-induced lattice relaxation. This optimized regime is characterized by grain-interior-dominated conduction and a nearly constant activation energy (~0.27–0.28 eV).

At high substitution (x = 0.10), ionic compensation becomes dominant. Excess oxygen vacancies, dopant clustering, and secondary phase segregation—particularly at grain boundaries—introduce deep trap states that interrupt hopping pathways, leading to strong carrier localization, sharply increased activation energy, and enhanced impedance. The Arrhenius behavior of DC conductivity confirms SPH as the primary transport mechanism across the measured temperature range, with the non-monotonic evolution of conductivity reflecting the transition from optimized hopping to disorder-driven localization at high La/Ce content.

3.5.5 Relationship between activation energy and defect chemistry

At the lowest substitution level (x = 0.02), the activation energy increases despite the introduction of charge carriers. This behavior is attributed to defect trapping rather than transport enhancement. At this stage, dopant ions mainly introduce local lattice distortions without forming continuous Fe^{2+}–Fe^{3+} hopping paths. Consequently, isolated Fe^{2+} states and vacancy-related defects act as localized traps, increasing the energy barrier for long-range charge transport.

As the substitution level increases to the intermediate range (x = 0.04–0.08), a percolative hopping network is gradually established. In this region, the Fe^{2+}/Fe^{3+} ratio reaches an optimal value, which minimizes carrier trapping and promotes efficient hopping. In addition, oxygen vacancies locally distort the Fe–O–Fe bond angles, thereby reducing hopping distances and facilitating charge transport. Under these conditions, grain interiors dominate the electrical response, while grain boundary resistance remains relatively low. As a result, the activation energy stabilizes in the range of approximately 0.27–0.28 eV, indicating an optimized small-polaron hopping environment.

At the highest substitution level (x = 0.10), the activation energy increases sharply. This behavior arises from excessive dopant incorporation, which leads to dopant clustering, secondary phase formation (such as CeO_2 and α-Fe_2O_3), and a high concentration of oxygen vacancies at grain boundaries. These effects disrupt continuous Fe^{2+}–Fe^{3+} hopping chains and introduce deep trap states, causing strong carrier localization. Consequently, both the activation energy and impedance response increase markedly at this composition.

3.5.6 Transport mechanism: dominance of small polaron hopping

The observed linear Arrhenius behavior of DC conductivity and the extracted activation energy values (0.25–0.30 eV for $x \leq 0.08$) are consistent with the small polaron hopping (SPH) model. In this mechanism, charge carriers are strongly coupled to lattice distortions and hop thermally between Fe^{2+} and Fe^{3+} ions at octahedral sites. Transport is therefore thermally activated and largely controlled by grain interiors at moderate substitution levels.

Although overlapping large polaron tunneling (OLPT) may contribute at higher frequencies, elevated temperatures, or intermediate substitution levels where wavefunction overlap increases, its role remains secondary. The

strong temperature dependence of DC conductivity and the magnitude of the activation energy indicate that SPH is the dominant transport mechanism within the studied temperature range.

The conductivity trends further suggest an increase in the density of states near the Fermi level from x = 0.02 to 0.06 due to Fe^{2+} formation, together with a reduction in effective hopping distance up to x = 0.08 as lattice disorder decreases. However, at x = 0.10, defect clustering leads to the collapse of effective hopping pathways. These observations are in good agreement with SPH-based models reported for rare-earth-substituted spinel ferrites.

In summary, charge compensation in La/Ce co-substituted $CoFe_2O_4$@$NiFe_2O_4$ nanocomposites is governed by a balance between Fe^{2+}-mediated electronic compensation and oxygen-vacancy-induced ionic disorder. The initial increase in activation energy originates from defect trapping, while its subsequent stabilization reflects the formation of an optimized Fe^{2+}/Fe^{3+} hopping network. Excessive substitution disrupts this balance, leading to carrier localization and increased resistivity. Overall, the electrical transport behavior is primarily controlled by small polaron hopping, with grain-boundary disorder and vacancy clustering dominating the response at high substitution levels.

3.5.7 Microstructural origin of Maxwell–Wagner polarization

The pronounced dielectric anomalies observed at high La/Ce substitution levels (x = 0.08–0.10) originate from MW polarization driven by microstructural heterogeneity and conductivity contrast within the H/S $CoLa_xCe_xFe_{2-2x}O_4$/$NiFe_2O_4$ ($x \leq 0.10$) SFNCs, rather than from an ideal core–shell architecture. Structural analyses reveal intergrown hard–soft nanodomains and agglomerated grains, which generate a high density of internal interfaces sufficient to promote interfacial charge accumulation. At low to intermediate substitution, La/Ce incorporation enhances Fe^{2+}/Fe^{3+} hopping in the $CoFe_2O_4$-rich phase, whereas excessive substitution ($x \geq 0.08$) induces defect accumulation, oxygen vacancies, and insulating secondary phases, leading to a strong conductivity mismatch between hard and soft regions. Additionally, nanometric grain size, dopant segregation, and secondary-phase localization render grain boundaries highly resistive, forming a classical MW configuration of conductive grains separated by insulating boundaries. The resulting interfacial polarization is corroborated by low-frequency impedance enhancement, pronounced ImZ/ImM features, and broadened relaxation behavior, with x = 0.10 marking a transition to grain-boundary-dominated transport and highly dispersive dielectric response.

3.5.8 Integrated analysis of electrical modulus and impedance formalisms

The integrated Z*–M* analysis therefore provides a physically unified picture: (i) Z* identifies *where* charge transport is blocked (i.e., resistive grain boundaries and interfaces), and (ii) M* reveals *how* charge carriers dynamically relax within a disordered energy landscape. At low substitution levels, both formalisms consistently indicate grain-dominated, near-Debye behavior. At high substitution, Z* highlights the dominance of resistive grain boundaries, while M* exposes the emergence of non-Debye relaxation arising from interfacial polarization and defect-induced energy dispersion. By combining both perspectives, the discussion avoids redundancy and instead demonstrates how impedance and modulus analyses converge to the same physical conclusion through different sensitivities. This integrated approach substantially strengthens the mechanistic interpretation of charge transport and dielectric relaxation in the studied H-S NCs and aligns the discussion with best practices in broadband dielectric spectroscopy.

3.5.9 Cole-cole impedance analysis

Each depressed semicircle in a Cole-Cole plot represents a dielectric relaxation process, typically modelled by a parallel resistor (R) and a constant phase element (*CPE*). A *CPE* is used instead of an ideal capacitor to account for the depressed nature of the semicircles, indicating a distribution of relaxation times due to material inhomogeneities. The high-frequency intercept of the semicircle on the *ReZ* axis represents the ohmic resistance, often associated with the grain resistance. The diameter of the semicircle represents the resistance of that particular relaxation process. The frequency at the *apex* of the semicircle (f_{apex}) is inversely related to the characteristic relaxation time ($\tau = 1/(2\pi f_{apex})$) [19, 49, 51]. Multiple semicircles indicate multiple distinct relaxation processes. The overall shift of the arcs towards the origin with increasing temperature signifies semiconducting behavior (decrease in resistance) and thermally activated relaxation processes. The impedance of a constant phase element (*CPE*) is defined as [49, 51–53].:

$$Z_{CPE} = \frac{1}{Q(j\omega)^n} \tag{3}$$

where Q is a constant associated with capacitance, $\omega = 2\pi f$ is the angular frequency, and n is the exponent characterizing the deviation from ideal capacitive behavior, with $0 \leq n \leq 1$. For an ideal capacitor, $n = 1$. In the case of a parallel $R\|$CPE circuit, the overall impedance is given by:

$$Z_{R\|CPE} = \frac{1}{1 + RQ\,(j\omega\,)^n} \tag{4}$$

The total complex impedance for the two-arc equivalent circuit model can be expressed as:

$$Z^* = R_s + \frac{R_g}{1 + R_g Q_g (j\omega\,)^{n_g}} + \frac{R_{gb}}{1 + R_{gb} Q_{gb} (j\omega\,)^{n_{gb}}} \tag{5}$$

where R_s is the series resistance, R_g and R_{gb} represent the grain and grain boundary resistances respectively, Q_g and Q_{gb} are the constant phase element parameters, and n_g and n_{gb} denote the exponents capturing the non-ideal capacitive behavior of the grain and grain boundary contributions.

Figure 14 presents the Cole–Cole (Nyquist) plots of complex impedance (−ImZ versus ReZ) for H/S $CoLa_xCe_xFe_{2-2x}O_4/NiFe_2O_4$ ($x \leq 0.10$) SFNCs, measured over the frequency range of 0–3 MHz and temperatures from 20 to 120 °C. For all compositions, the impedance spectra exhibit depressed semicircular arcs, indicating non-Debye relaxation behavior arising from a distribution of relaxation times associated with structural and microstructural heterogeneity. The systematic reduction in arc diameter with increasing temperature reflects a decrease in bulk and grain-boundary resistances, confirming thermally activated semiconducting conduction.

For the undoped sample (x = 0.00), a single depressed semicircle is observed at all temperatures, suggesting that grain and grain-boundary responses are strongly overlapped and cannot be distinctly resolved. As La/Ce co-substitution increases to x = 0.02 and 0.04, the arc diameter increases substantially, particularly at low temperatures, indicating enhanced resistive behavior. This increase is attributed to lattice distortion, defect generation, and enhanced carrier scattering induced by aliovalent La^{3+}/Ce^{3+} substitution at Fe sites, which increases the effective potential barriers for charge transport.

At intermediate substitution (x = 0.06), the impedance spectra still display a single dominant semicircle; however, the total resistance decreases relative to x = 0.04, suggesting a partial compensation between defect-induced localization and thermally assisted hopping conduction. The persistence of a single arc implies that grain and grain-boundary contributions remain convoluted in this compositional regime.

A marked change in impedance behavior emerges at higher substitution levels (x = 0.08 and 0.10). For x = 0.08, the Nyquist plots exhibit a distorted semicircle accompanied by a low-frequency tail, particularly at lower temperatures. This feature signifies the onset of resolvable grain-boundary relaxation and enhanced interfacial polarization. The irregular shape reflects increased electrical heterogeneity and a broad distribution of relaxation times caused by non-uniform grain-boundary resistances and defect clustering.

At the highest substitution level (x = 0.10), two distinct depressed semicircular arcs are clearly evident, especially at low temperatures. The high-frequency arc corresponds

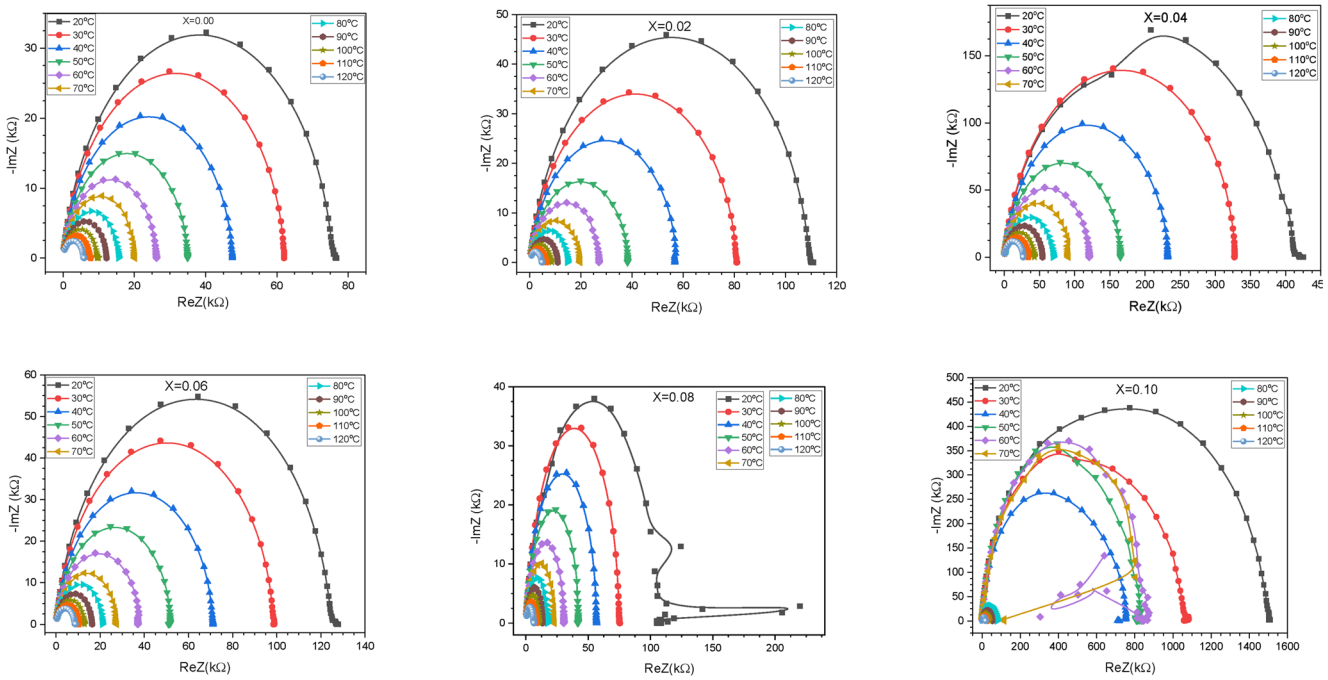


Fig. 14 The Cole-Cole plot of complex impedance of H/S $CoLa_xCe_xFe_{2-2x}O_4/NiFe_2O_4$ ($x \leq 0.10$) SFNCs for range of 0–3 MHz range

to grain response, while the large low-frequency arc arises from grain-boundary relaxation. The exceptionally large arc diameter and high ReZ intercept indicate that grain-boundary resistance dominates the overall impedance, confirming the formation of highly resistive interfacial barriers. This behavior is characteristic of strong MW polarization arising from charge accumulation at grain–grain boundary interfaces in a highly heterogeneous H–S ferrite system. With increasing temperature, both arcs contract significantly, reflecting enhanced carrier mobility and reduced barrier height. Mostly, the evolution of the Cole–Cole plots with composition demonstrates a clear transition from bulk-dominated transport at low La/Ce contents to grain-boundary-controlled conduction at high substitution levels. The emergence of distinct grain and grain-boundary relaxation processes at $x \geq 0.08$ highlights the critical role of interfacial polarization and electrical heterogeneity in governing the dielectric and impedance response of H/S $CoLa_xCe_xFe_{2-2x}O_4/NiFe_2O_4$ ($x \leq 0.10$) SFNCs.

In summary, the Cole-Cole plots provide compelling evidence of temperature-dependent dielectric relaxation processes and the profound influence of La and Ce substitution on the electrical properties of H/S $CoLa_xCe_xFe_{2-2x}O_4/NiFe_2O_4$ ($x \leq 0.10$) SFNCs. The clear resolution of grain and grain boundary contributions at higher substitution ratios, especially $x = 0.10$, is a critical finding, indicating highly resistive grain boundaries that dominate charge transport. Simulating these plots with appropriate equivalent circuits would allow for precise quantitative analysis of the underlying electrical parameters and their temperature dependencies.

The electrical transport in the H/S $CoLa_xCe_xFe_{2-2x}O_4/NiFe_2O_4$ ($x \leq 0.10$) SFNC systems is governed by the hopping of charge carriers between ions of the same element, but different valence states located at equivalent lattice sites. The La^{3+} and $Ce^{3+/4+}$ ions' co-substitution has a double role in this process. First, because of their large ionic radii, La and Ce ions have the preference to occupy the octahedral [B] sites, displacing some Fe^{3+} ions to the tetrahedral (A) sites. This redistribution will alter the Fe^{2+}/Fe^{3+} concentration at the B-sites, which are the primary pathways for polaron hopping. Secondly, the RE-ions' co-substitution introduces a mismatch in the size that generates lattice strains, which high possibly lead to the creation of oxygen vacancies for charge compensation. These vacancies, along with the segregated RE-ions at grain boundaries, act as dipole centers that enhance MW interfacial polarization. This can explain the prominent relaxation peaks observed in the electric modulus (Im*M*) and impedance (Im*Z*) spectra for higher *x* values, where the accumulation of charges at the interfaces between the hard and soft phases becomes the dominant mechanism.

3.5.10 Cole–cole impedance fitting analysis

Figure 15 shows the Nyquist plots of complex impedance for La/Ce co-substituted H-S $CoLaCe_xFe_{2-2x}O_4@NiFe_2O_4$ SFNCs ($x \leq 0.10$) measured at 30°Cover the frequency range of 0–3 MHz. The impedance spectra were satisfactorily fitted using the equivalent circuit model R(CR)(QR)(CR), and the extracted electrical parameters are summarized in Table 6. This model effectively separates the contributions arising from grains, grain boundaries, and interfacial regions, enabling a detailed Cole–Cole analysis of electrical transport and polarization mechanisms.

For low La/Ce substitution levels ($x = 0.00$–0.04), the impedance response is dominated by grain effects. R_g is extremely high or approaches infinity, while C_{gb} remains negligible. In this composition range, the frequency exponent *n* remains close to unity ($n \approx 0.88$–0.89 for $x = 0.00$ and 0.02), indicating nearly ideal Debye-type relaxation. This behavior suggests that charge transport is mainly governed by electron hopping between Fe^{2+} and Fe^{3+} ions within the ferrite lattice, with minimal influence from interfacial polarization. The corresponding Cole–Cole plots are therefore weakly depressed semicircles, reflecting a relatively narrow distribution of relaxation times and limited structural heterogeneity.

At $x = 0.04$, a pronounced deviation from ideal behavior is observed, as evidenced by the drastic reduction of the frequency exponent ($n \approx 0.04$). This anomaly indicates strong dispersion of relaxation times and marks the onset

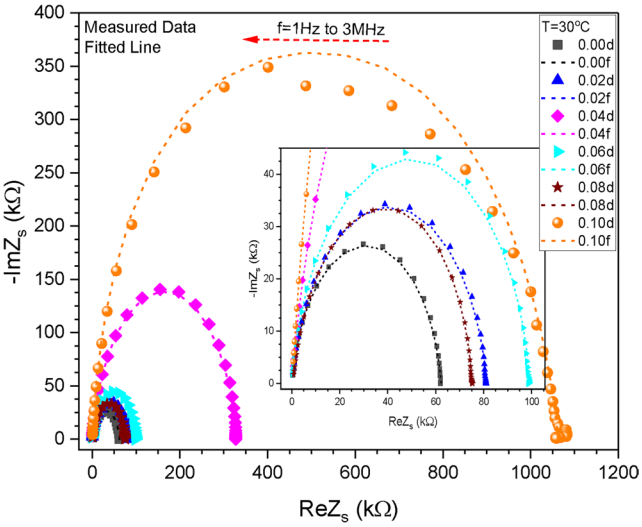


Fig. 15 Nyquist plots of the complex impedance (-ImZ-ReZ) for H/S $CoLa_xCe_xFe_{2-2x}O_4@NiFe_2O_4$ SFNCs ($x \leq 0.10$) measured at 30 °C over the frequency range of 0–3 MHz. (The solid lines represent fits obtained using the proposed EEC, illustrating the respective contributions of grain, grain-boundary, and interfacial components to the overall impedance response.)

Table 6 Fitted Nyquist (Cole–Cole) parameters obtained from the R(CR)(QR)(CR) EEC model for H/S $CoLa_xCe_xFe_{2-2x}O_4$@$NiFe_2O_4$ SFNCs ($x \leq 0.10$), measured at 30 °C over the frequency range of 0–3 MHz. (The extracted parameters quantify the contributions of grains, grain boundaries, and interfacial regions to the overall electrical transport and polarization behavior)

Ratio, x	0.00	0.02	0.04	0.06	0.08	0.10
R_s [Ω]	0	50	4.1	97.2k	73.7k	1.2 m
C_g[F]	∞	∞	∞	9.3 m	34.7 m	414p
R_g[Ω]	9.75G	9.75G	0	2.9 M	601.6k	0.3µ
CPE, Yo[S-sec^n]	192p	171p	2.3µ	4.4 m	20.5 m	68p
Freq power, *n*	0.89	0.88	0.04	0.86	0.56	0.90
R_q[Ω]	62.3k	81.2k	∞	1271	2 m	1.04 M
C_{gb}[F]	0	0	∞	1.2 m	4.3 m	149.2
R_{gb}[Ω]	0	0	9.75G	1.95 M	9.44 M	159 M

Where 0:too small; ∞:too big; p:pico; µ:micro; m:milli; k:kilo; M:Mega; G:Giga

of electrical heterogeneity within the system. Such behavior can be attributed to the initial formation of defect states, lattice distortion, and local compositional disorder induced by La^{3+}/Ce^{3+} incorporation, which begin to disrupt the uniform grain conduction mechanism.

With further increase in La/Ce content ($x \geq 0.06$), a clear transition from grain-dominated to grain-boundary- and interface-dominated conduction is observed. R_s and R_{gb} increase sharply, reaching values on the order of 0.1–1 MΩ and higher (Table 6). Simultaneously, C_{gb} increases significantly, particularly for $x = 0.06$ and 0.08, indicating enhanced charge accumulation at interfacial regions. This behavior is characteristic of Maxwell–Wagner interfacial polarization, arising from the strong conductivity contrast between grains and grain boundaries, as well as between the hard $CoFe_2O_4$ and soft $NiFe_2O_4$ phases.

The evolution of the constant phase element (CPE) parameters further confirms the non-ideal relaxation behavior at higher substitution levels. The increase in CPE admittance (Y_0), together with the deviation of n from unity ($n \approx 0.56$–0.86 for $x = 0.06$–0.08), reflects a broad distribution of relaxation times associated with interfacial polarization, defect-induced carrier trapping, and space-charge effects. Consequently, the Cole–Cole semicircles in Fig. 15 become increasingly depressed, indicating enhanced electrical inhomogeneity and the coexistence of multiple relaxation processes.

At the highest substitution level ($x = 0.10$), the frequency exponent partially recovers ($n \approx 0.90$), suggesting a redistribution of charge carriers and partial stabilization of interfacial regions. However, the very high resistance and capacitance values indicate that electrical transport remains strongly governed by grain-boundary and interfacial effects rather than bulk conduction.

Predominantly, the Cole–Cole analysis based on Fig. 15; Table 6 demonstrate that La/Ce co-substitution effectively tunes the electrical transport behavior of $CoFe_2O_4$@ $NiFe_2O_4$ NCs from grain-controlled, quasi-Debye conduction at low substitution levels to interfacial and grain-boundary-dominated transport at higher *x* values. The enhanced MW polarization and non-Debye relaxation at elevated La/Ce contents provide a consistent and intrinsic explanation for the dielectric and impedance anomalies observed in the system, highlighting the crucial role of compositional engineering in modulating interfacial polarization and electrical functionality in H-S SFNCs.

4 Conclusion

H-S $CoLaCe_xFe_{2-2x}O_4$@$NiFe_2O_4$ SFNCs ($x \leq 0.10$) were successfully synthesized via a one-pot sol–gel auto-combustion route, and their phase formation and nanostructure were confirmed by XRD, SEM, TEM, and HR-TEM. The results demonstrate that La/Ce co-substitution in the Co-ferrite hard phase critically controls the electrical and dielectric response of these hard–soft nanocomposites.

Dielectric spectroscopy reveals strong frequency dispersion and temperature-dependent behavior arising from thermally activated hopping conduction, space-charge effects, and defect-assisted relaxation. With increasing La/Ce content, the dielectric loss evolves from bulk-dominated behavior to relaxation-dominated dissipation, particularly at $x \geq 0.08$, indicating enhanced interfacial polarization. Impedance spectroscopy provides direct evidence for a transport crossover from grain-controlled to grain-boundary-dominated conduction at high substitution levels. At $x = 0.10$, the appearance of multiple semicircular arcs and equivalent circuit fitting confirm a pronounced increase in grain-boundary resistance. Electric modulus analysis further reveals strongly non-Debye relaxation, reflecting a broad distribution of relaxation times induced by cationic disorder and interfacial heterogeneity.

An optimal substitution range ($x \approx 0.04$–0.08) is identified, where charge transport is enhanced through thermally assisted small-polaron hopping and dielectric performance is maximized. Excessive substitution ($x = 0.10$) leads to structural disorder, rare-earth segregation, and insulating

grain boundaries, resulting in suppressed conductivity and dominant Maxwell–Wagner polarization. Overall, La/Ce co-substitution is shown to be an effective strategy for grain-boundary engineering and controlled tuning of dielectric relaxation in hard–soft ferrite nanocomposites, offering clear design guidelines for high-frequency, EMI-shielding, and energy-related electronic applications.

Author contributions (A) Baykal: Methodology, Conceptualization, Investigation, Supervision, Writing – original draft, Writing – review & editing. (B) Unal: Investigation, Formal analysis, Writing – original draft, Writing – review & editing. M.A. Almessiere: Methodology, Formal analysis, Resources. A. Demir Korkmaz: Investigation, Formal analysis, Resources, Writing – original draft, Writing – review & editing. Y. Slimani: Investigation, Formal analysis, Writing – original draft, Writing – review & editing.

Funding Open access funding provided by the Scientific and Technological Research Council of Türkiye (TÜBİTAK).

Data availability Data will be made upon request from the corresponding author.

Declarations

Conflict of interest The authors declare that they have no known competing financial interests or personal relationships that could have appeared to influence the work reported in this paper.

Open Access This article is licensed under a Creative Commons Attribution 4.0 International License, which permits use, sharing, adaptation, distribution and reproduction in any medium or format, as long as you give appropriate credit to the original author(s) and the source, provide a link to the Creative Commons licence, and indicate if changes were made. The images or other third party material in this article are included in the article's Creative Commons licence, unless indicated otherwise in a credit line to the material. If material is not included in the article's Creative Commons licence and your intended use is not permitted by statutory regulation or exceeds the permitted use, you will need to obtain permission directly from the copyright holder. To view a copy of this licence, visit http://creativecommons.org/licenses/by/4.0/.

References

1. S. Hema, S. Sambhudevan, Ferrite-based polymer nanocomposites as shielding materials: a review. Chem. Pap. **75**, 3697 (2021)
2. K. Dhabekar, K.M. Kant, Structural and dielectric properties of cobalt ferrite-based nanocomposites. Physica B **603**, 412752 (2021)
3. O. Crisan, I. Dan, P. Palade, A.D. Crisan, A. Leca, A. Pantelica, Magnetic phase coexistence and hard–soft exchange coupling in FePt nanocomposite magnets. Nanomaterials. **10**(8), 1618 (2020)
4. A. Rahmana, R. Jayaganthan, Study of $CoFe_2O_4$/$NiFe_2O_4$ nanocomposite ferrite film. Surf. Eng. **33**(11), 1 (2017)
5. K. Malaie, M.R. Ganjali, Spinel nano-ferrites for aqueous supercapacitors; linking abundant resources and low-cost processes for sustainable energy storage. J. Storage Mater. **33**, 1020 (2021)
6. P. Thakur, S. Jangra, F. Wan, B. Ravelo, A. Thakur, Chapter: Introduction to Spinel Nano-Ferrites, in *Applications of Spinel-Nanoferrites*. ed. by A. Takur, P. Thakur (Taylor Francis Print, 2025)
7. J.S. Kounsalye, A.S. Dive, A.V. Humbe, P.G. Undre, Chapter: Advances in Magnetic Materials, in ed. by A.R. Kadam, K.R. ZAkde, S.J. Dhoble, H.C. Swart (CRC Press, 2025)
8. G. Katoch, R. Himanshi, J. Jasrotia, A. Prakash, A. Verma, S.K. Kandwal, R. Godara, V. Verma, G. Raja, Kumar, Crystal structure, synthesis, properties and potential applications of cobalt spinel ferrite: A brief review, Materials Today: Proceedings. https://doi.org/10.1016/j.matpr.2023.03.585
9. S. Sagadevan, Z.Z. Chowdhury, R.F. Rafique, Preparation and characterization of nickel ferrite nanoparticles via co-precipitation method. Materials Research **21**(2), e20160533 (2018)
10. O. Manner, S. Sarmah, K.P. Patra, D. Maji, S. Ravi, T. Bora, Effect of rare earth (Ho and Er) co-substitution on the magnetic and dielectric properties of nanocrystalline cobalt ferrites. Ceram. Int. **50**, 30912–30930 (2024)
11. S. Ikram, J. Jacob, K. Mehboob, K. Mahmood, N. Amin, M.I. Arshad, M.A. Nabi, Role of rare earth metal ions doping on structural, electrical, magnetic, and dielectric behavior of spinel ferrites: a comparative study. J. Supercond. Nov. Magn. **34**, 1833 (2021)
12. S. Masoudpanah, S.S. Ebrahimi, M. Derakhshani, S. Mirkazemi, Structure and magnetic properties of La substituted $ZnFe_2O_4$ nanoparticles synthesized by sol–gel auto combustion method. J. Magn. Magn. Mater. **370**, 122 (2014)
13. K. Muthuraman, V. Naidu, S.K.A. Ahmed, T. Vasudevan, Study of electrical and magnetic properties of cerium doped nano smart magnesium ferrite material. Int. J. Comput. Appl. **65**, 18 (2013)
14. M.I.U. Haq, A.U. Rehman, M. Asghar, M.U. Nabi, N. Amin, S. Tahir, M.I. Arshad, Influence of Ce^{3+} and La^{3+} substitution on structure, optical parameters and electrical behavior on Mg-Zn ferrites synthesized via co-precipitation method. J. Supercond. Nov. Magn. **35**, 719 (2022)
15. M.A. Almessiere, Y. Slimani, A.D. Korkmaz, A. Baykal, H. Güngüneş, H. Sözeri, S.E. Shirsath, S. Güner, S. Akhtar, A. Manikandan, Impact of La3 + and Y3 + ion substitutions on structural, magnetic and microwave properties of Ni0.3Cu0.3Zn0.4Fe2O4 nanospinel ferrites synthesized: via sonochemical route. RSC Adv. **9**, 30671–30684 (2019)
16. V. Ludhiya, N. Hari Kumar, A. Edukondalu, D. Ravinder, Solution combustion synthesis of nanostructured Mg0.5Ni0.3Cu0.2CexFe2-xO4 ferrites: structural, optical and electromagnetic properties. Appl. Phys. A **129**, 614 (2023)
17. T. Khatoon, N. Alam, V.S. Chandel, A. Azam, S. Srivastava, J. Gupta, Exploring the synergistic effects of La^{3+} substitution on dielectric performance of manganese cobalt ferrite: implications for advanced electronic applications. Ceram. Int. **50**, 7156–7167 (2024)
18. K. Dhabekar, K.M. Kant, Soft/hard ferrite nanocomposites: evaluation of temperature dependent dielectric properties. Physica B **627**, 413581 (2022)
19. P. Sivaprakash, S. Divya, S. Esakki Muthu, A. Ali, Z. Jaglicic, T.H. Oh, I. Kim, Effect of rare earth Europium (Eu^{3+}) on structural, morphological, magnetic and dielectric properties of $NiFe_2O_4$ nanoferrites. Mater. Sci. Eng., B **301**, 117200 (2024)
20. S. Roostaei, H. Ansarinejad, E.A. Dawi, F.H. Alsultany, S.K. Issa, M. Ahmadi-Kashani, M. Salavati-Niasari, Sol–gel auto-combustion synthesis of a novel ternary magnetic-recyclable $ZnFe_2O_4$/ZnO/CeO_2 nano-photocatalyst for highly efficient visible-light-induced degradation of organic contaminants. Appl. Water Sci. **15**, 193 (2025)
21. M. Amiri, M. Salavati-Niasari, A. Akbari, T. Gholami, Removal of malachite green (a toxic dye) from water by cobalt ferrite silica magnetic nanocomposite: herbal and green sol-gel autocombustion synthesis. Int. J. Hydrogen Energy. **42**, 248 (2017)

22. C. Pahwa, S.B. Narang, P. Sharma, Composition dependent magnetic and microwave properties of exchange-coupled hard/soft nanocomposite ferrite. J. Alloys Compd. **815**, 152391 (2020)
23. N.S. Al-Bassami, S.F. Mansour, E. Abdel-Fattah, M.A. Abdo, Ce-Co-Mn-Zn ferrite nano catalyst: a synergetic effect of rare earth Ce^{3+} on enhanced optical properties and photocatalysis. Ceram. Int. **49**(12), 20601 (2023)
24. O. Manner, T. Bora, Investigation of the magnetic and dielectric properties of rare earth (Ho, Er) Co-substitution in stoichiometry modified cobalt ferrites nanocrystals. Mater. Chem. Phys. **348**, 131522 (2026)
25. O. Manner, D. Maji, K.P. Patra, S. Ravi, T. Bora, Enhanced dielectric and soft magnetic properties of rare earth (Sm, Er) co-substituted cobalt ferrites nanocrystals. Mater. Chem. Phys. **339**, 305 (2025)
26. Y. Slimani, M.A. Almessiere, S. Guner, B. Aktas, S.E. Shirsath, M.V. Silibin, A.V. Trukhanov, A. Baykal, Impact of Sm^{3+} and Er^{3+} cations on the structural, optical, and magnetic traits of spinel cobalt ferrite nanoparticles: comparison investigation. ACS Omega **7**, 6292–6301 (2022)
27. O. Manner, D. Maji, K.P. Patra, S. Ravi, T. Bora, Enhanced dielectric and soft magnetic properties of rare earth (Sm, Er) co-substituted cobalt ferrites nanocrystals. Mater. Chem. Phys. **339**, 130746 (2025)
28. I.O. Alade, Y. Zhang, X. Xu, Modeling and prediction of lattice parameters of binary spinel compounds (AM_2X_4) using support vector regression with Bayesian ptimization. New J. Chem. **45**, 15255–66 (2021)
29. Y. Zhang, X. Xu, Machine Learning Lattice Constants for Spinel Compounds. Chem. Phys. Lett. **760** (2020) 137993
30. Y. Zhang, X. Xu, Predicting the thermal conductivity enhancement of nanofluids using computational intelligence. Phys. Lett. A **384**(20), 126500 (2020)
31. Y. Zhang, X. Xu, Machine learning the central magnetic flux density of superconducting solenoids. Mater. Technol. **37**(4), 272–279 (2022)
32. Y. Zhang, X. Xu, Predicting magnetic remanence of NdFeB magnets from composition. J. Supercond. Novel Magn. **34**, 2711–2715 (2021)
33. A. Hashhash, M. Kaiser, Influence of Ce-substitution on structural, magnetic and electrical properties of cobalt ferrite nanoparticles. J. Electron. Mater. **45**, 462 (2016)
34. A. Teber, M.F. Sarac, Electrical, magnetic, microstructural, and characteristic properties of zirconium-substituted $Co_{0.5}Ni_{0.5}Zr_xFe_{2-x}O_4$ spinel ferrite nanostructures. Arab. J. Sci. Eng. **48**, 8153 (2023)
35. M. Jurča, L. Munteanu, J. Vilčáková, J. Stejskal, M. Trchová, J. Prokeš, I. Křivka, Core–shell inorganic/organic composites composed of polypyrrole nanoglobules or nanotubes deposited on MnZn ferrite microparticles: electrical and magnetic properties. J. Compo. Sci. **8**(9), 373 (2024)
36. P. Pascariu, A. Airinei, M. Asandulesa, A. Rotaru, Insights into the optical, magnetic and dielectric properties of some novel polysulfone/$NiFe_2O_4$ composite materials. Polym. Int. **67**(9), 1313 (2018)
37. J. Zhai, N. Cai, Z. Shi, Y. Lin, C.W. Nan, Magnetic-dielectric properties of $NiFe_2O_4$/PZT particulate composites. J. Phys. D Appl. Phys. **37**(6), 823 (2004)
38. N. Ponpandian, P. Balaya, A. Narayanasamy, Electrical conductivity and dielectric behaviour of nanocrystalline $NiFe_2O_4$ spinel. J. Phys. Condens. Matter **14**(12), 3221 (2002)
39. A.U. Rehman, S. Sharif, H.H. Hegazy, N. Morley, N. Amin, M. Akhtar, M.I. Arshad, Z. Farooq, Z. Munir, T. Munir, Low dielectric loss, and enhanced magneto-dielectric properties of $Cu_{0.5}Cd_{0.5-x}$ Co_x Fe_2O_4 ferrites via Co^{2+} substitution. Mater. Today Commun. **34**, 105371 (2023)
40. M. Kamran, M. Anis-ur-Rehman, Influence of La^{3+} substitutions on structural, dielectric and electrical properties of spinel cobalt ferrite. Ceram. Int. **49**(4), 7017 (2023)
41. F.A. Sheikh, H.M.N.H.K. Asghar, M. Khalid, Z.A. Gilani, S.M. Ali, N.H. Khan, M.A. Shar, A. Alhazaa, Synthesis of Ce^{3+} substituted Ni-Co ferrites for high frequency and memory storage devices by sol-gel route. J. Alloys Compd. **938**, 168637 (2023)
42. R.A. Mondal, B.S. Murty, V.R.K. Murthy, Maxwell–Wagner polarization in grain boundary segregated NiCuZn ferrite. Curr. Appl. Phys. **14**(12), 1727 (2014)
43. H. Kaur, A.K. Tyagi, A. Singh, D.S. Ahlawat, Dielectric, magnetic, and structural investigation of Cr substituted cobalt nanoferrite via auto-combustion. J. Mater. Sci. Mater. Electron. **34**, 2143 (2023)
44. Y. Bakış, I.A. Auwal, B. Ünal, A. Baykal, Conductivity and dielectric properties of $SrLa_xBi_xY_xFe_{12-3x}O_{19}$ ($0.0 \leq x \leq 0.33$) hexaferrites. Ceram. Int. **42**, 11780 (2016)
45. Y. Bakıs, I.A. Auwal, B. Ünal, A. Baykal, Maxwell-Wagner relaxation in grain boundary of $BaBi_xLa_xY_xFe_{12-3x}O_{19}$ ($0.0 < x < 0.33$) hexaferrites. Composites Part B **99**, 248 (2016)
46. S. Akhtar, M.A. Almessiere, B. Ünal, A. Demir Korkmaz, Y. Slimani, N. Tashkandi, A. Baykal, A. Ul-Hamid, A. Manikandan, Electrical and dielectric properties of $Ni_{0.5}Co_{0.5}Ga_xFe_{1.8-x}O_4$ ($x \leq 1.0$) spinel ferrite microspheres. J. Rare Earths **41**(2), 259 (2023)
47. Q. Ni, L. Sun, E. Cao, W. Hao, Y. Zhang, L. Ju, Enhanced magnetic and dielectric properties of $NiFe_2O_4$ ferrite ceramics co-substituted by (Li^+, Zn^{2+} and La^{3+}). Ceram. Int. **46**(7), 9722 (2020)
48. Y. Slimani, B. Ünal, A. Baykal, M.A. Almessiere, A. Thakur, K.M. Batoo, Unraveling the dielectric and electrical properties of binary $BaTiO_3/Ba_{0.98}Ca_{0.01}Mg_{0.01}Fe_{12}O_{19}$ composites. J. Phys. Chem. Solids **191**, 112047 (2024)
49. R.S. Yadav, I. Kuˇritka, J. Vilcakova, J. Havlica, J. Masilko, L. Kalina, J. Tkacz, J. ˇSvec, V. Enev, M. Hajdúchov´a, Impact of grain size and structural changes on magnetic, dielectric, electrical, impedance and modulus spectroscopic characteristics of $CoFe_2O_4$ nanoparticles synthesized by honey mediated sol-gel combustion method. Adv. Nat. Sci. Nanosci. Nanotechnol. **8**, 045002 (2017)
50. K. Alamelu Mangai, K. Tamizh Selvi, M. Priya, P. Sureshkumar, M. Rathnakumari, Impedance and modulus spectroscopy studies of cobalt substituted strontium hexaferrite ceramics. J. Mater. Sci. Mater. Electron. **28**, 13445 (2017)
51. N.B. Velhal, N.D. Patil, A.R. Shelke, N.G. Deshpande, V.R. Puri, Structural, dielectric and magnetic properties of nickel substituted cobalt ferrite nanoparticles: effect of nickel concentration. AIP Adv. **5**(9), 097166 (2015)
52. M. Kamran, M.A. Rehman, Study of dielectric and electrical properties in Co-(Fe–Ce-Nd) nanosized spinel ferrites. Mater. Sci. Semicond. Process. **153**, 107111 (2023)
53. R. Qindeel, N.H. Alonizan, Structural, dielectric and magnetic properties of cobalt based spinel ferrites. Curr. Appl. Phys. **18**(5), 519 (2018)
54. J. Song, J. Zhang, A.R. Zada, Y. Ma, K. Qi, $CoFe_2O_4/NiFe_2O_4$ S-scheme composite for photocatalytic decomposition of antibiotic contaminants. Ceram. Int. **49**(8), 12327 (2023)
55. S. Saha, K.L. Routray, Structural, magnetic, and dielectric properties of Terbium substituted nanosized Nickel-Ferrites from a new perspective. J. Sol-Gel Sci. Technol. **111**, 566 (2024)

Publisher's Note Springer Nature remains neutral with regard to jurisdictional claims in published maps and institutional affiliations.